CENTRO INTERNACIONAL DE ESTUDOS
DE DOUTORAMENTO E AVANZADOS
DA USC (CIEDUS)

TESIS DE DOCTORADO

THE IMPACT OF WAVE NUMBER SELECTION AND SPIN-UP TIME IN SPECTRAL NUDGING

Breogán Xacobo Gómez Hombre

ESCUELA DE DOCTORADO INTERNACIONAL
PROGRAMA DE DOCTORADO EN ENERGÍAS RENOVABLES Y SOSTENIBILIDAD ENERGÉTICA

SANTIAGO DE COMPOSTELA
AÑO 2019

USC
UNIVERSIDADE
DE SANTIAGO
DE COMPOSTELA

CENTRO INTERNACIONAL DE ESTUDOS DE DOUTORAMENTO E AVANZADOS DA USC (CIEDUS)

DECLARACIÓN DEL AUTOR DE LA TESIS

The impact of wave number selection and spin-up time in spectral nudging

D. Breogán Xacobo Gómez Hombre

Presento mi tesis, siguiendo el procedimiento adecuado al Reglamento, y declaro que:

1) *La tesis abarca los resultados de la elaboración de mi trabajo.*
2) *En su caso, en la tesis se hace referencia a las colaboraciones que tuvo este trabajo.*
3) *La tesis es la versión definitiva presentada para su defensa y coincide con la versión enviada en formato electrónico.*
4) *Confirmo que la tesis no incurre en ningún tipo de plagio de otros autores ni de trabajos presentados por mí para la obtención de otros títulos.*

En Exeter, 5 de marzo de 2019

Fdo.

USC
UNIVERSIDADE
DE SANTIAGO
DE COMPOSTELA

CENTRO INTERNACIONAL DE ESTUDOS DE DOUTORAMENTO E AVANZADOS DA USC (CIEDUS)

AUTORIZACIÓN DEL DIRECTOR / TUTOR DE LA TESIS

The impact of wave number selection and spin-up time in spectral nudging

D. Gonzalo Miguez Macho

INFORMA:

Que la presente tesis, corresponde con el trabajo realizado por D. Breogán Xacobo Gómez Hombre, bajo mi dirección, y autorizo su presentación, considerando que reúne los requisitos exigidos en el Reglamento de Estudios de Doctorado de la USC, y que como director de ésta no incurre en las causas de abstención establecidas en Ley 40/2015.

En Santiago de Compostela, 11 de marzo de 2019

Fdo. Gonzalo
Miguez
Macho

To: Selma, Carolina, Elías and Sabela.

If I have learned one thing from this project, it is that you are what matters me the most.

Table of contents

Acknowledgments

This has been a long and exhausting project and, through the years it took me to finish this document, I had been lucky to get the amazing support of relatives, friends and colleagues. This has been a long period of time and it implies that there are many people to mention, I apologize in advance for anyone that I might have forgotten.

My first and most special thanks are for my wife Selma and our children Carolina, Elías and Sabela. They have seen me in my best and worst moments and yet they always have showed me their unconditional support. This work has happened thanks to their love and caring.

I want to thank my family, and specially my parents Puri and Gonzalo, who have continuously supported me during this process. They are going to feel some relief when seeing me finally finishing this. Also my brother Brandán for so many nice chats that helped to distract me, I wish they could had happen more often and with some beers in front of us, instead that on the phone. A very special thanks to Judith, who has gone through the same experience as mine and understood this effort better than anyone else, Marcelino, for his support and advice that hopefully will allow me become “superior” one day, and of course Andrea, Tiago, Antón, Sebas, Marta, Martita, María and Manuela. And finally, my two grandparents Chelo and Papi, who sadly are not here to see this and would have enjoyed it more than anyone else.

I want to thank my managers Vicente, Richard and Chris for supporting me in sharing my work responsibilities with the demanding tasks associated with this project. I thank my colleagues at MeteoGalicia and the Met Office for their support every time I needed to spell out my frustrations. I also want to thank all the PhD students at the non-linear physics group, for creating such a nice and warm working environment, it was so great to share the afternoons with you. Finally, my thanks to all the people at CESGA, and particularly to Carlos and Pablo, for their invaluable help when running my experiments.

I want to give special thanks to my friend and team colleague Cristina, who has reviewed and corrected the greater part of this manuscript substantially improving its quality (this section is the only one you have not reviewed and I am sure that, at this point, you have already found something that can be improved!). I also want to thank George Efstathiou from the University of Exeter, and Erasmo Buonomo and Segolene Berthou from the Hadley Centre for reviewing my work and providing suggestions on how to interpret my results and improve their discussion.

Finally, I want to thank my PhD advisor, Gonzalo, for his scientific guidance throughout this process, and for showing me the difference between a scientist and a researcher. It took a bit of time but I hope I am getting there.

PROJECTS AND INSTITUTIONS

I want to mention the Earth2Observe project from the 7th Framework Programme (ref. 603608) of the European Commission, the Ministerio Español de Economía y Competitividad (CGL2013-45932-R) and the European Regional Development Fund (ERDF) for funding this research. The E-OBS dataset from the EU-FP6 project ENSEMBLES (http://ensembles-eu.metoffice.com) and the data providers in the ECA&D project (http://www.ecad.eu). And Elsa Cattani from Consiglio Nazionale delle Ricerche (Italy, National Research Council) and NASA for providing the data used for verification. Plots have been created using Matplotlib (Hunter, 2007).

1 Introduction to spectral nudging

1.1 STATE OF THE ISSUE

Nudging, in its many variations, has been widely used for many applications in numerical weather prediction. Essentially, this technique relaxes the solution of a differential equation towards a reference value, which is considered the truth, at any given grid point. It is expected that the surrounding grid points will accommodate to this reference value and, hence, give a more realistic result, consistent at the same time with the physical equations of the model. One of nudging's first applications was in data assimilation (Anthes, 1974), and although nowadays different, more complex, techniques are being used for this purpose, nudging was once operational in weather forecast centres for global models such as the Met Office (Lyne et al., 1982) and regional models also at the Met Office (Bell, 1986) and the Deutsche Wetterdienst (Schraff, 1996, 1997).

When a gridded analysis is available, nudging is generally applied throughout the model domain, constraining the solution by the reference fields at all points (Davies and Turner, 1977; Stauffer and Seaman, 1990). In recent years, a variation of nudging called spectral nudging (Miguez-Macho et al., 2004; von Storch et al., 2000; Waldron et al., 1996) has gained popularity. Here, only a part of the spectrum of a variable is relaxed to the equivalent part of the spectrum of a reference field. In most applications, only the larger scale is nudged, and the model complements the solution providing the smaller scales.

One common application of spectral nudging is regional climate downscaling (Miguez-Macho et al., 2004, 2005; von Storch et al., 2000), where an estimate of the global circulation (e.g. a global reanalysis) is used as boundary condition for a Regional Climate Model (RCM). It is well known that if the RCM has a large grid, the solution can diverge significantly from the global analysis (Davies, 1976, 1983), and the longer waves within the domain, which are not handled correctly by the imposed boundary conditions, reflect at the boundaries

and perturb the circulation elsewhere (Miguez-Macho et al., 2004). Spectral nudging prevents the RCMs from departing from its boundary conditions while still allowing the model to generate its own local features (Miguez-Macho et al., 2004, 2005). Some authors (Braun et al., 2012; Colin et al., 2010; de Elía et al., 2008; de Elía and Côté, 2010; Lucas-Picher et al., 2013; Sanchez-Gomez et al., 2009) tested the impact of spectral nudging on regional climate modelling, showing that it reduces the model internal variability. Other works (Berg et al., 2013; Radu et al., 2008) demonstrated nevertheless that the smallest scales that are not driven by spectral nudging are not significantly affected by scale interaction. More recently, it was showed that spectral nudging improves the estimation of the frequency of tropical cyclones in a hurricane season due to a better representation of the large-scale patterns, particularly the low-level monsoon circulation (Choi and Lee, 2016).

Spectral nudging has also been used for various other applications: reduce near surface wind errors by nudging a reference field above the PBL (Vincent and Hahmann, 2015), improve the simulation of a tropical typhoon (Wang et al., 2013), recover small scale features in a geostrophic two layer model when it is nudged to a large-scale field (Katavouta and Thompson, 2013), improve the simulation of an eddy field when the model is relaxed to observed climatology (Stacey et al., 2006), ameliorate the modelled cloud field (Meinke et al., 2006) and preserve the model's solution while allowing local turbulence to develop (Yamaguchi et al., 2013). Spectral nudging has also been used for data assimilation applications (Stauffer et al., 1991; Stauffer and Seaman, 1994).

1.2 MOTIVATION

In all of the presented works, the values for cut-off wave-numbers are selected depending on researcher's preferences. Some authors select the minimum wave number possible, thereby nudging the longest scales alone (Miguez-Macho et al., 2004) ensuring that a minimum interference with the LAM's dynamics occurs. Other authors use a value related to their simulation's purposes or the field they are nudging to. For example, in a particular work it is chosen to nudge scales longer

than 1500 km based on the length scale that is intended to be evaluated (Separovic et al., 2012); in other, to nudge scales larger than 2000 km, as this is the effective resolution of the model used as boundary condition (Liu et al., 2012); and in another work, to nudge scales larger than 300 km, as this is the typical resolution of a GCM (Omrani et al., 2013). When testing different configurations, some authors noted that the most appropriate cut-off wave number for their particular application corresponded to a length scale range around 1000 km (Liu et al., 2012; Wang and Kotamarthi, 2013). Particularly, in Liu et al. (2012), some sensitivity tests were conducted to evaluate the differences between grid nudging and spectral nudging, although the set of variables was not the same in both techniques. This shows that a criteria has not been established in the scientific community on which is the most appropriate cut-off value when designing an experiment.

In this work we investigate two features of the spectral nudging technique that have not yet been explored in detail. First, the impact of selecting different cut-off wave numbers in the model's results, with particular emphasis on the effect in the spectral structure of the solution. Our results show that this parameter can have a decisive impact in the model solution and yet, there are not guidelines to select a sensible value. In the course of our experiments, we also study a second parameter, the spin-up time needed before the solution of the LAM (limited area model) reaches a balance with the nudging forcing. If the times are too short the model might not benefit for the nudging contribution while if it is too long, the error accumulation can overrun and contaminate the results. The first parameter is particularly important when using spectral nudging for dynamic climate downscaling and the second is very relevant when studying individual weather events or when spectral nudging is used as a *poor man's* data assimilation technique.

Our work is organised as follows, in Chapter 2 we describe the different nudging techniques used, including spectral nudging and grid nudging. Mid and tropical latitudes have different synoptic dynamics, for this reason we have studied them in separate works. In Chapter 3 we present our results for a domain located in South West Europe and

we also describe our analysis methodology in full detail, meanwhile in Chapter 4 we apply the same analysis on the modelling of hurricanes for a domain centred in the Gulf of Mexico. In Chapter 5 we study the suitability of spectral nudging as an initialisation technique to mimic the role of a data assimilation. Finally, in Chapter 6 we give a summary of our findings.

2 Nudging techniques

In *Nudging*, or Newtonian relaxation, the model solution is relaxed towards a reference value, generally considered better than the model's original solution. We use two different variations of nudging, known as grid nudging and spectral nudging, and in this section, we describe their general formulation and the fundamental differences between both techniques.

The WRF modelling system is used for all experiments in this work, and since its nudging implementation is based on Stauffer and Seaman (1990), for simplicity we follow the same notation. There, nudging is defined as:

$$\frac{\partial \alpha}{\partial t} = F(\alpha,\vec{x},t) + G_\alpha W(\vec{x},t)\varepsilon(\vec{x})(\hat{\alpha}_0 - \alpha) \qquad (1)$$

Where: $F(\alpha,\vec{x},t)$ is the tendency predicted from the atmospheric model, $\vec{x}$ represent the independent spatial variables *(x, y, z)*, $\alpha(\vec{x},t)$ represents a particular variable of our model's state, $\hat{\alpha}_0$ is the value towards where we want to nudge our field (i.e. an analysis or an observation) which is typically time-interpolated to the modelling time, G_α is the nudging coefficient that represents the relative magnitude of the nudging term related to the rest of model process included in $F(\alpha,\vec{x},t)$, $W(\vec{x},t)$ is a time dependent weight (typically used to nudge observation at a certain time) and $\varepsilon(\vec{x})$ is an analysis quality factor (typically between 0 and 1).

If one assumes that $\varepsilon(\vec{x}) = 1$ (perfect analysis), $W(\vec{x},t) = 1$ (no time dependent weight) and, for simplicity, drops the physical forcing terms from *(1)*, the following expression is obtained.

$$\frac{\partial \alpha}{\partial t} = G_\alpha(\hat{\alpha}_0 - \alpha) \qquad (2)$$

This has the solution,

$$\alpha = \hat{\alpha}_0 + (\alpha - \hat{\alpha}_0)e^{-G_\alpha t} \quad (3)$$

Where α_i is the value of α at the start of the nudging process. Therefore, the model state approaches the analysis with e-folding time $T_{G_\alpha} = 1/G_\alpha$. Typically, a value similar to $3{\cdot}10^{-4}$ s^{-1} (roughly 1 h^{-1}) is chosen.

2.1 GRID NUDGING

The WRF modelling system used for our experiments, has a slightly different version of *(1)* that does not consider the quality of the analysis $\varepsilon(\vec{x})$ and adds a vertical weight factor $V(\vec{x})$, ranging between 1 and 0. In many nudging applications, some kind of vertical weight is applied to remove the impact near the surface, so that the LAM develops its own circulation near the surface while dynamics in the upper levels are dominated by the boundary condition model. The nudging equation, as implemented in WRF, is expressed by:

$$\frac{\partial \alpha}{\partial t} = F(\alpha,\vec{x},t) + G_\alpha W(\vec{x},t)V(z)(\hat{\alpha}_0 - \alpha) \quad (4)$$

The model solution is nudged towards a field (typically, the same providing lateral boundary conditions) that is first interpolated to the LAM's grid. Then equation *(4)* is applied as if we had a *perfect observation* at the same grid point.

2.2 SPECTRAL NUDGING

Spectral nudging follows a similar strategy to that of grid nudging. Starting from equation *(4)*, a spectral filtering is applied to $(\hat{\alpha}_0 - \alpha)$, first in the X direction, and then in the Y direction. No filtering is applied in the vertical direction. Spectral nudging is therefore expressed as:

$$\frac{\partial \alpha}{\partial t} = F(\alpha,\vec{x},t) + G_\alpha W(\vec{x},t)V(z)Filt_{xy}[(\hat{\alpha}_0 - \alpha)] \quad (5)$$

Where $Filt_{xy}$ represents a spectral filtering above a certain cut-off wave number. To perform the filtering, i) each row of $(\hat{\alpha}_0 - \alpha)$ is

transformed to the spectral space using a FFT algorithm, ii) all wave numbers above a certain X-direction cut-off wave-number are set to zero and, iii) the remaining Fourier coefficients are then back transformed to spatial space using an inverse FFT. The process is then repeated to each column using a Y-direction cut-off wave-number. FFT algorithm assumes a periodic field and a LAM is typically very similar to its boundary condition at the boundaries, ensuring that $(\hat{\alpha}_0 - \alpha)$ is periodic along a column or row.

Spectral filtering $Filt_{xy}$ removes all spatial frequencies higher than those corresponding to the selected cut-off wave number, ensuring than solely the longer wavelengths in $(\hat{\alpha}_0 - \alpha)$ are used for nudging. Because of the orthogonality of the functions of the Fourier expansion, only the same spectral components of the physical space term $F(\alpha,\vec{x},t)$ in *(5)* are affected by nudging. Note that when the cut-off wave number is the highest possible for a given domain, the $Filt_{xy}$ term in *(5)* yields a full FFT followed by an inverse FFT, thus making the spectral nudging procedure exactly equal to grid nudging (with the exception of the precision lost after the two operations). For this reason, grid nudging can be considered an asymptotic case of spectral nudging, as it is simply spectral nudging to the full spectrum, and results from the upcoming chapters will show the validity of this affirmation.

3 The impact of wave number selection and spin-up time in mid latitudes

3.1 INTRODUCTION

In this chapter we perform a systematic study of the impact of spectral nudging on the model solution in a mid-latitude setting. Particularly, we evaluate how the cut off wave number and spin up time affect the error and structure of the forecasted fields. As a result, we suggest which are the most appropriate values in terms of performance and error reduction.

This chapter is organized as follows, in Section 3.2 we describe the experiments, in Section 3.3 we present results and in Section 3.4 we discuss the impact of nudging on an example case, finally, in Section 3.5 a summary of our findings is given.

Results from this chapter have been published at the Quarterly Journal of the Royal Meteorological Society (Gómez and Miguez-Macho, 2017)

3.2 EXPERIMENTAL SET-UP

3.2.1 Model description and configuration

The Advanced Research WRF (ARW) modelling system (Skamarock and Klemp, 2008), version 3.5, is used in this work with a single domain set-up than covers Southern Europe with 119x105

Parameterisation	Scheme	Reference
Micro-physics	WRF Single Moment 6-class	(Hong and Lim, 2006)
Long wave radiation	RRTM	(Mlawer et al., 1997)
Short wave radiation	Dudhia	(Dudhia, 1989)
Surface layer	MM5 similarity	(Skamarock et al., 2008)
Land surface	5-layer thermal diffusion	(Skamarock et al., 2008)
PBL	Yonsei University	(Hong et al., 2006)
Cumulus	Kain-Fritsch	(Kain, 2004)

Table 1: Physic parameterisations used in the WRF modelling set-up

horizontal points at 36 km resolution and 33 vertical levels (Figure 1). The most relevant physical parameterizations employed are shown in Table 1. Initial and boundary conditions are provided by NCEP Global Atmospheric Analysis (GDAS) at 3 hour frequency.

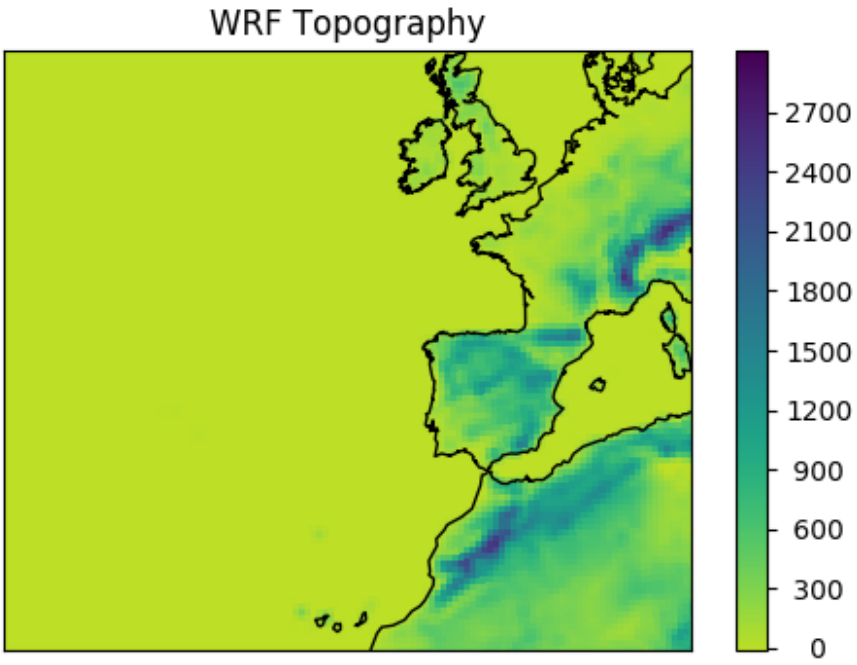

Figure 1: Model topography (meters) for the domain used in all experiments from Chapter 3

Nudging is active in all simulations, except for the free run experiments. Generally, it is not recommended to nudge humidity and temperature in the PBL because the surface characteristics of the LAM (e.g. topography) can be rather different from those in the global analysis used as boundary condition; therefore, we only nudge these variables above the WRF estimation for PBL height. Wind is nudged in the full column. The WRF modelling system (version 3.7 and below) does not have the option to nudge humidity spectrally, so we have implemented this capability in our version of the model. Spectral nudging is mostly used for climate downscaling purposes, where

moisture budgets are a fundamental result from the simulations. For this reason, and for others related to the strong gradients, both vertical and horizontal, of the moisture fields and the lack of accuracy in global reanalysis in representing them, moisture nudging is in general not considered. Our experiments are only four days in duration, within the short to medium range NWP, and, since moisture budgets are not of particular concern, to fully explore the nudging capability, we choose to nudge specific humidity in addition to potential temperature and the wind components. We do not nudge geopotential height as we assume that nudging to the wind components provides a similar benefit. The nudging coefficient is set to a common value of $3 \cdot 10^{-4}$ s^{-1}, equivalent to 1 h^{-1}. Experiments have also been performed with coefficients of 3 h^{-1} and 6 h^{-1} with similar results.

3.2.2 Experiments

For analysis, we select three monthly periods: i) June 2010, that was anomalously warm with frequent convective precipitation in Southern Europe, ii) September 2011, when cold fronts and high pressure situations alternate, and iii) January 2013, with continuous cold fronts passing over the Iberian Peninsula and a particular intense explosive cyclogenesis event. They correspond to a wide range of typical atmospheric circulation conditions for summer, fall and winter, respectively, of mid-latitudes in the North Atlantic, and are therefore suitable for drawing conclusions about the general behaviour of the model's solution with spectral nudging.

The goal of the experiments is to perform a statistical study of the impact of the wave number selection and the spin-up time in the model results when using spectral nudging. For each day of the selected monthly period, we run a 4 day simulation with spectral nudging activated and we repeat this simulation 8 times changing the cut-off wave number. In addition, we run another two simulations, one with no nudging (free run) and one with grid nudging, to a total 10 simulations per day, which implies that around 300 runs are performed per monthly period. From the results, we evaluate how the model separates from its boundary condition as the simulation advances.

Table 2 shows the cut-off wave numbers selected and their corresponding wavelength dimensions in both directions. The selection of wave numbers pairs in X and Y is such that the represented scales are similar in each direction. In Table 2, we also include the grid nudging and the free run experiments, which correspond to nudging in the full spectrum and no nudging at all, respectively. Results indicate that indeed it is reasonable to consider grid nudging and free run as asymptotic cases of spectral nudging.

3.3 RESULTS

We compare the results from the monthly runs against NCEP's GDAS analyses, with similar resolution to that of the WRF domain. Contrasting WRF output with its boundary condition allows us to study how the LAM separates from its forcing and, particularly, at which scales this separation happens. In addition, we compare model results with ERA interim to perform a verification against an independent field and to investigate how model error changes with different spin-up times and nudging configurations. Both GDAS and Era interim are interpolated to the WRF domain and all statistics are calculated on a grid point basis every 6h. We note that both GDAS and ERA-interim are interpolated twice before used, first when they are taken from their spectral model grid to the rectangular grid for public dissemination, and second, when they are interpolated to the lambert conformal WRF grid

Exp	Nudging	WN_X	WN_Y	Length X	Length Y
FR 5000	Free run	No Spectrum		4284	3780
SP 2000	Spectral	3	3	2124	1872
SP 1300	Spectral	4	4	1416	1248
SP 1000	Spectral	5	5	1062	936
SP 750	Spectral	7	6	708	750
SP 500	Spectral	9	8	531	535
SP 375	Spectral	12	11	386	374
SP 250	Spectral	18	16	250	250
SP 175	Spectral	25	22	177	178
GR 75	Grid	Full Spectrum		72	72

Table 2: Nudging configuration for each experiment. Wave numbers correspond to a Fourier series where 1 represents the non-oscillatory term of the FFT. This follows the criteria used in the WRF implementation.

of our experiments. These interpolations, both in the horizontal and the vertical, destroy and distort any high frequency information in GDAS or ERA interim, yielding basically noise at small scales. When grid nudging or spectral nudging with a high wave number are used, the model solution is forced towards unphysical fields at the small scale, thereby imposing local imbalances in the flow. The result is a certain unexpected behaviour of WRF, such as the slight loss of amplitude with respect to GDAS at the finer scales observed in power spectra of the GN experiments. It is therefore undesirable to introduce nudging of any strength in the small-scale part of the spectrum.

All calculations in this section are performed directly on model levels and for the prognostic nudged variables: specific humidity, wind (kinetic energy) and potential temperature. Results are very similar for the three monthly periods chosen; therefore we only present results for 2011, to avoid redundancy. Wind is presented as kinetic energy to summarize the information in both components into one single variable; theta and relative humidity plots are generally omitted, as the behaviour of both variables is similar to that of kinetic energy.

3.3.1 Power spectrum

To evaluate how the different nudging configurations affect the spectral structure of the WRF solution, we calculate the power spectrum for the different variables. For each model lead time and level we perform the FFT for each row in the x-direction and we average the square of the amplitude Fourier coefficients for all of the rows. We repeat the process for each of the 30 simulations in the considered monthly period. A similar calculation is carried out for all columns in the y-direction and, as a result, for a given month, we obtain a power spectrum per level, forecast time, variable and direction (X and Y). Since the FFT needs to be performed on periodic data, which is not the case of the rows and columns of our model solution, we de-trend the model fields following the methodology proposed by Errico (1985). The linear trend between the first and the last element of a column/row is calculated and then it is removed from all elements, preserving the spectral structure of the field. Then, the FFT is applied and, finally, the power spectrum is plotted in decibels. The latter operations can be

summarized in the expression $log(<a_i^2>)/20$, where $log()/20$ is the conversion to decibels, a_i denotes the amplitude of the $i-th$ harmonic

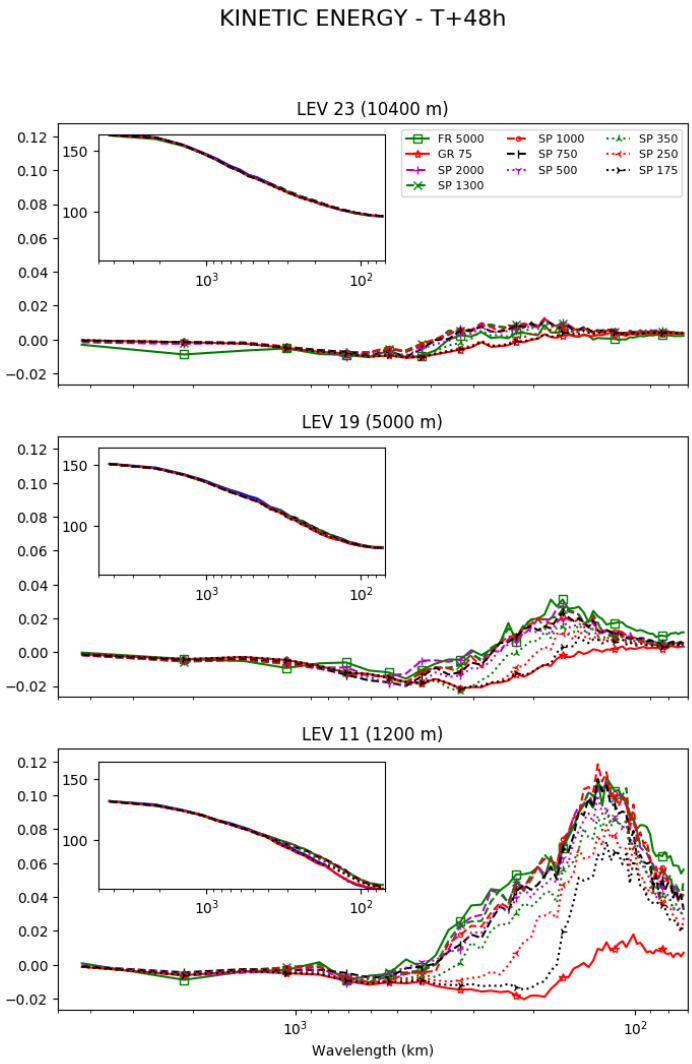

Figure 2: Kinetic energy power spectra (db) for all experiments (insert) and their fractional differences against GDAS at modelling lead time 48 h (main) for model sigma levels 11, 19 and 23. Results correspond to October 2011 experiments.

and the angle brackets represent the expectation (average) over all model runs at a specific level, forecast time and row/column. The first element of the FFT series, which is a non-oscillatory term, is omitted in all plots.

Power spectra calculated in X or Y direction do not show any significant difference, and for this reason, we only show those in the X direction. The insets in Figure 2 depict the power spectrum for the kinetic energy at 48 h, when we assume that the solution has reached a balance between the nudging forcing and the model internal climate (see Section 3.3.2 for further justification). Power spectrum for 12 h has also been calculated, with similar results (not shown). Results are shown for model sigma levels 11, 19 and 23 (around 1.200 m, 5.000 m and 10.400 m above the model's surface, which roughly correspond to 850 hPa, 500 hPa and 300 hPa over the ocean). Dotted curves correspond to the experiments nudging different parts of the spectrum and solid lines to grid nudging (red) and free run (green). The divergence among the experiments is very small, especially at the larger scales, which makes it difficult to assess the impact on each scale.

The larger plot in each figure represents the power spectrum for the relative difference of each experiment against GDAS. The grid nudging experiment curves (red solid) hover around zero, indicating that there is practically no difference in their spectral structure with GDAS, except perhaps at the smallest length scales, where WRF is able to generate some high frequency information not present in the analysis. These differences at the fine scale are, in any case, minimal when compared with those in other experiments. The free run experiment (green, solid curves), as expected, exhibits the largest difference against GDAS, which starts to be relevant only around scales of 800 km and smaller. The similarity in the larger scales is explained by the fact that we are evaluating results at 48 h from initialization, when the synoptic patterns are still relatively close to the boundary conditions from GDAS. As we decrease the part of the spectrum that is being nudged, the different spectral nudging experiments show a transitional behaviour between grid nudging and free run. The curves are close to grid nudging spectrum up to the cut-off wave number, and then

converge to the free run experiment thereafter. This confirms that spectral nudging is effectively altering the spectral shape of the WRF solution, making it rather equal to GDAS for the longer wave lengths below the cut-off wave number and very similar the free run experiment above it, in the small scale part of the spectrum. As the cut-off wave number moves to higher frequencies, the WRF solution is not able to fully reach the spectral shape of the free run solution for kinetic energy; however it does so remarkably well for the rest of the variables (not shown). The results for the different levels show that the impact of the nudging on the model solution is largest close to the surface and smaller in the upper troposphere.

3.3.2 Root mean squared distance

To investigate how the WRF diverges from its boundary condition as the simulation advances we calculate the root mean squared distance between the forecast model and GDAS and ERA Interim for each model grid point at each lead time, level and variable. This is repeated for each one of the experiments on Table 2. Results are shown in Figure 3, again, for model levels 11, 19 and 23.

When comparing WRF simulations against its boundary condition (GDAS, Figure 3, left) we note that the simulation without nudging (free run, green curves) has the largest RMSD and it separates from the boundary condition steadily as the lead time increases. In simulations extending to 8 days (not shown) we observed that the distance between NCEP and the free run simulation grows at a much slower rate, suggesting that WRF reaches its own climate beyond the 4 days shown. The grid nudging experiment (red curves) has in general the lowest RMSD of all experiments and follows a flat line that is close to 0, which means that in this simulation WRF is not able to generate any independent solution, at any scale, and it simply mimics GDAS's values. The RMSD of all nudging experiments reaches a constant value after some spin-up time. Most of the gain occurs in the first 24 hours, then slowly ramps until hour 40 and thereafter a constant distance is maintained until the end of the simulation. This is particularly true for specific humidity at higher levels for experiments with spectral nudging and longer cut-off wave lengths (not shown). In general, experiments

nudging lower wave number pairs have larger RSMD, but the difference with GDAS is at best about half of what it is for the free run experiment, and as mentioned before, the growth flattens out much earlier on. Below level 11 (not shown) temperature and humidity have a more erratic behaviour and grid nudging does not necessarily have the smallest distance to GDAS, reflecting the fact that nudging is not being applied below the PBL. The impact of the diurnal cycle is very apparent

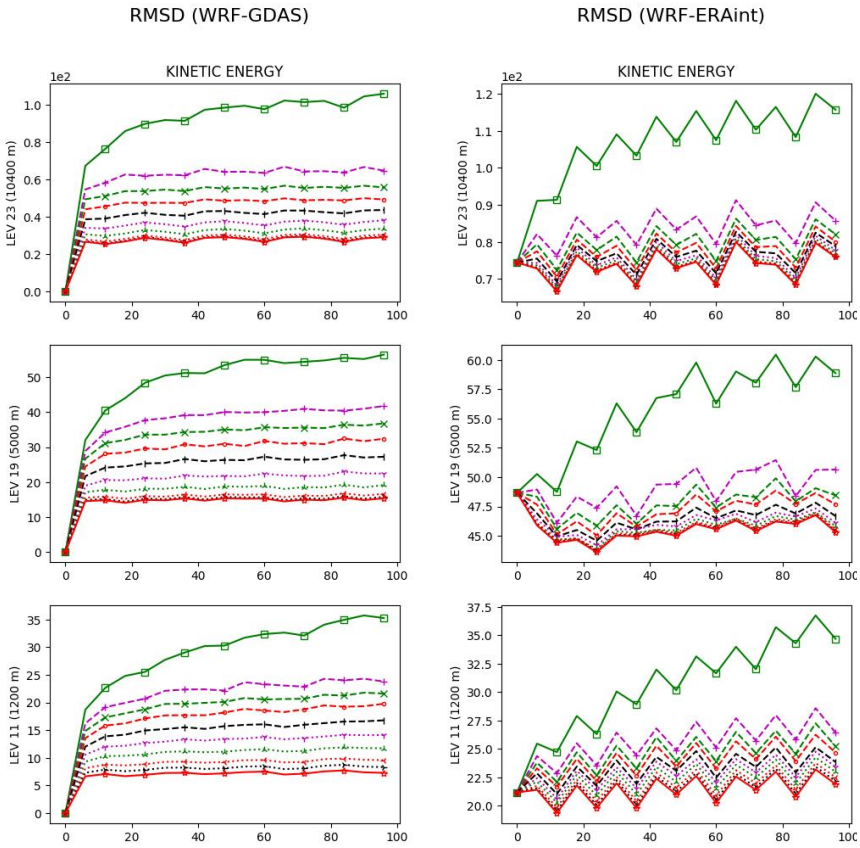

Figure 3: Root mean square distance between WRF and GDAS (left) and between WRF and Era interim (right) versus forecast time for kinetic energy (J). Results correspond to October 2011 experiments and model sigma levels 11, 19 and 23. Colours and symbols of the curves are as in Figure 2.

on the RMSD in the lower troposphere, and, although it is clear that the model separates from GDAS more than in upper levels, the distance is still constant, even if the nudging does not have the same strength as in the rest of the column.

The RMSD against ERA interim (Figure 3, right) shows a similar behaviour to the RMSD against GDAS, but with slightly higher values. We speculate that this is caused by the fact that the model solution stays at a constant distance to GDAS and hence the model´s RMSD to ERA Interim is indirectly showing the climatic distance between both atmospheric analyses. The saw tooth pattern of the curves is likely linked to a diurnal oscillation of the bias in ERA interim (Bao & Zhang, 2013). If we consider ERA interim as an independent, verifying truth, these plots can be interpreted as the actual error, or RMSE, of the WRF solution. In all nudging experiments the model's RMSD to ERA Interim stays at a constant value, but the spin-up time is different depending on the variable. Similarly to the RSMD with GDAS, most variables reach an equilibrium distance against ERA interim in between 12 hours and 24 hours forecast lead time, except specific humidity, which takes more than 40 hours (not shown). In contrast, the spectral nudging experiments do not represent such a gradual transition in the WRF solution from grid nudging to free run as in the comparison with GDAS, and have now an RMSD much closer to the grid nudging values at all times. Results from the spectral analysis in Section 3.3.1 suggest that the high frequency modes are responsible for the variations in RMSD among the different experiments. As the cut-off wave numbers for spectral nudging get smaller, the WRF solution is able to produce its own higher frequency modes that differ from GDAS and ERA interim. This implies that an increase in the RMSD does not necessarily translate into a degradation in WRF performance, but reflects the lack of ability of the reference fields to reproduce the finer details. We conclude that the cut-off wave number for spectral nudging should be selected so that it ensures that the large scale is tailored to the reference fields but not so large as to suppress the small scales, which are the true contribution of the LAM to the solution. In the next section we investigate the range of values for the cut-off wave number that fulfil these premises.

3.3.3 RMSD vs. cut-off wavenumber

In this section we examine the behaviour of the RMSD against GDAS and ERA interim as we change the cut-off wave number in the nudging experiments. Figure 4 (a, c) represents the RMSD at 48 h from WRF against both analyses as a function of the wavelength of the cut-off wavenumber selected in the nudging experiments (see Table 2 for a list of the associated wavelengths). Calculations are shown at the same levels used in the previous sections. Free run and grid nudging experiments do not have an associated cut-off wave number, thus we use the value of the full domain's length for the former and twice the grid resolution for the latter, as this is the smallest wave that it is possible to reproduce (inverse of the Nyquist frequency) with the model's solution. Results from previous sections suggest that to consider grid nudging and free run asymptotic cases of spectral nudging is a reasonable approach. Finally, we plot results at 48 h as we assume that at this time the model is fully spun up and the error characteristics do not change significantly any further in time. As in previous sections, only results for FFT performed in the X-direction are shown, as those with the FFT performed in the Y-direction are very comparable. Only results for one of the monthly periods (2011) are discussed for the same reasons.

The RMSD in Figure 4 (a, c) decreases very quickly for the longer wave lengths, suggesting that most of the improvement in the RMSD is obtained from nudging the synoptic scales. The slope of the curve changes sharply at around the 1000 km wave length and it nearly flattens out completely for smaller values thereafter. This shows that almost no benefit is obtained from increasing the cut-off wavenumber toward the small scale part of the spectrum and, in agreement with the discussions in previous sections, any small increment there comes at the expense of damping the high frequency contribution from WRF. Ideally, the nudging cut-off wave numbers in the model simulation should be around the *inflexion point in the tendency*, whereby a large part of the synoptic error is reduced, yet the finer detail is not damped.

To estimate an approximate value for the point where the tendency in the RMSD curves changes, we fit two linear functions to the four

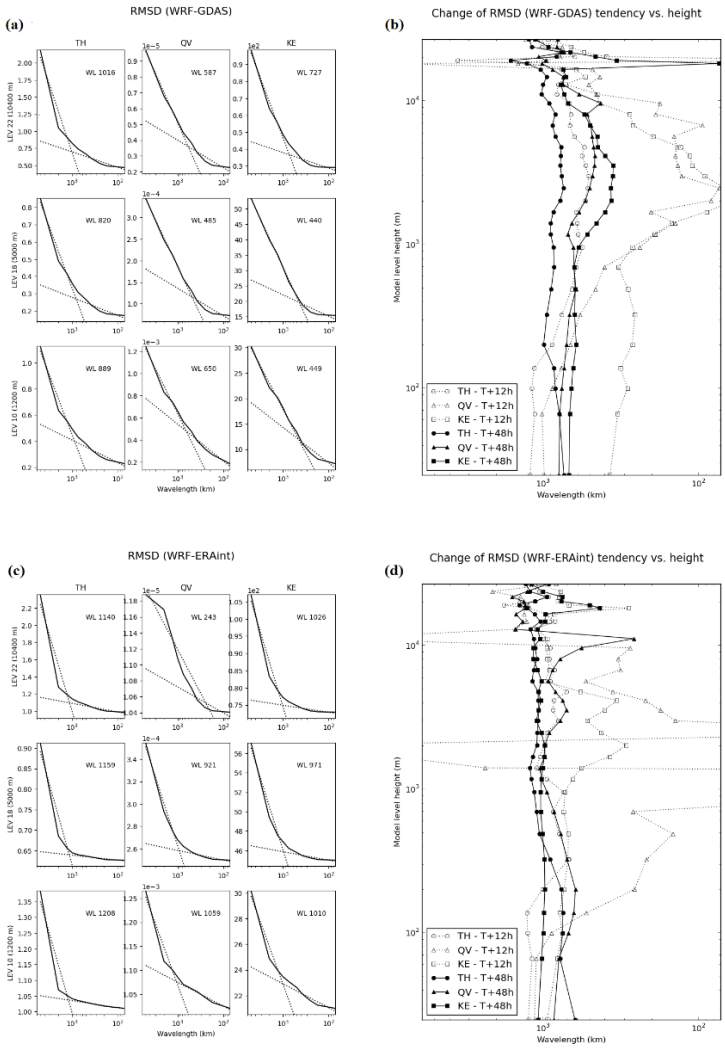

Figure 4: Root mean square distance against WRF-GDAS (a) and WRF-ERA-Int. (c) versus cut-off wavelength. Panels a & c show results for theta (Kelvin), specific humidity (kg kg^{-1}) and kinetic energy (J) and for model sigma levels 11, 19 and 23. The WL numbers shown in each plot correspond to the wavelength of the inflection point in the trends of the curves. Panels b and d depict WL numbers versus model level for the different variables at 12 h (dotted) and 48 h (solid) forecast lead time.

outermost points on each side of the curve and find the crossing point (Figure 4, a, c). The crossing points for each variable and each model level are represented in Figure 4 (b, d). Additionally, to complement these plots we have also included the inflexion points of the tendency for 12 h. Results against GDAS show that, first, the lines at 12 h present a more erratic behaviour than those at 48 h, supporting the idea that the simulation needs longer times to spin-up; and second, once the model is spun-up there is a consistent behaviour in the vertical, with the change in tendency occurring between 500 km and 1000 km depending on the variable.

When comparing with ERA interim, the vertical profiles of the inflexion points in the tendency present a more erratic behaviour at 12 h than against GDAS, but, after 48 h, the lines are remarkably smooth from bottom to top. This is particularly true for the energy, which stays at a value of a 1000 km wave length up to a 10 km height. This indicates once more that a spin-up time of at least 48 h is needed to ensure a consistent behaviour of the error throughout the column. The change of tendency occurs at somewhat larger wave lengths than when WRF is compared to GDAS.

Perhaps unsurprisingly, this value of 1000 km coincides with the Rossby Radius of Deformation, the length scale at which rotational effects become as important as buoyancy or gravity wave effects in the evolution of the flow about some disturbance (Gill, 1982). The Rossby Radius of Deformation is commonly defined as $R=Nh/f$, where N is the Brunt–Väisälä frequency, f is the Coriolis parameter and h is the scale height of the system. When h is taken to be the average height of the tropopause at mid-latitudes, R has an approximate value of 1000 km, which indicates the typical length scale of the meso-scale synoptic systems. The Rossby Radius has been broadly described in the literature and it can be interpreted as the transition area from the synoptic scale to the convective scale. Boundary conditions in LAMs do not handle properly the synoptic scales, and disturbances of that size generate reflections at the borders and interferences with the solution within the domain that greatly affect the quality of the results (Miguez-Macho et al., 2004). Shorter wavelength disturbances, associated with

convective scales, are however effectively damped by the relaxation zone at the boundaries. Our results show that nudging scales longer than the Rossby Radius, efficiently eliminates most error growth related to the interactions of the modelled long waves with the imposed boundary values, whereas the model still develops high resolution features as in simulations with no nudging at all. The Rossby Radius is therefore the reference value for the cut-off wave number in spectral nudging. Since it depends on latitude, different values may be selected depending on the location of the region of interest.

3.4 EXAMPLE CASE

To illustrate the impact of nudging and the choice of different cut-off wavenumbers on particularly challenging episodes, in terms of

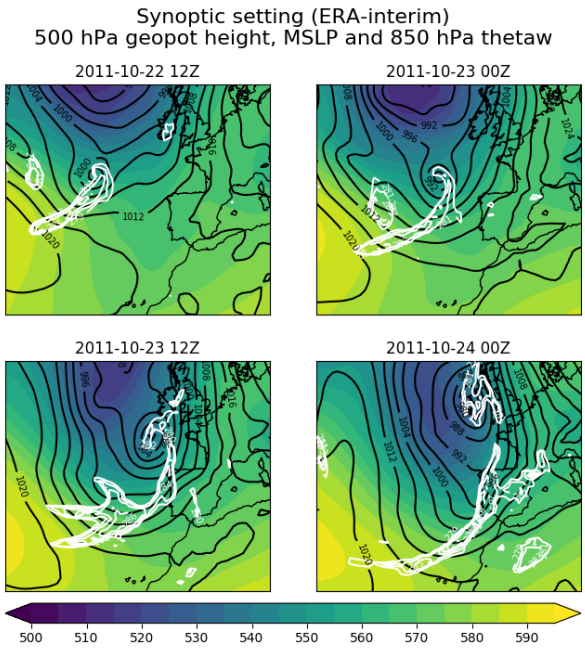

Figure 5: Era Interim mean sea level pressure (mb, black contour), 850 hPa wet bulb potential temperature (Kelvin, white contour) and 500 hPa geopotential height (dm, shaded) every 12 h from 2011-10-21 12Z to 2011-10-24 00Z showing the synoptic setting for the example case.

model forecasting skills, we discuss here the case of a complex synoptic system that produced an extreme precipitation event over the Atlantic Coast of the Iberian Peninsula on 23rd October, 2011. As for any of the days in the monthly periods, 10 experiments are run for the episode, with different wave number cut-off values for spectral nudging, detailed in Table 2. Simulations start October 21th, 2011, 2.5 days before the focus period on October 23rd.

3.4.1 Synoptic setting

Figure 5 shows the general synoptic setting of the case. On October 22 at 12Z, a high pressure system in mainland Europe blocks the westward progress of a cyclone in the North Atlantic, southwest of Iceland. At this time, wave development is occurring in the low level baroclinic zone associated to the trailing part of the cold front, on the southern flank of the main cyclone. 12 hours later, at 00Z October 23, this wave becomes a closed low approaching the Iberian Peninsula, while a second incipient wave is also developing behind. The first secondary cyclone deepens as it moves north towards Ireland, so that at 12Z, the general low pressure area in the North Atlantic has at the surface two centres and a developing wave. The former main and first secondary cyclone merge over Ireland, as the incipient cyclone developing from the second wave approaches the west coast of the Iberian Peninsula at 00Z on October 24th.

The extreme precipitation event over Galicia and Portugal evolved from this complex situation. Figure 6 shows mean sea level pressure from ERA-interim (contour) and precipitation rate (mm/hr) from TRMM (3B42) satellite product at 3 h intervals for October 23 (shaded). Each field from TRMM, which is provided every 3 hours in mm/hr, is best interpreted as the precipitation rate effective at the nominal observation time (Huffman et al., 2007) so the fields are first interpolated to hourly values and then accumulated to 3 hourly precipitation. The interaction of the front associated to the first secondary cyclone, reaching Galicia at 12Z and the forming front from the cyclogenesis associated to the second wave, occurring west of the Iberian Peninsula between 12Z and 21Z (T+60 and T+69, respectively),

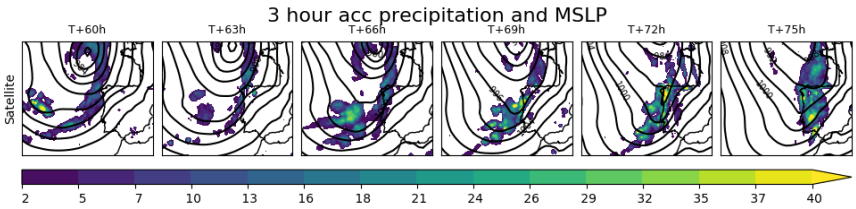

Figure 6: Era Interim mean sea level pressure (mb, contour) and TRMM (3B42) 3 hour accumulated precipitation (mm, shaded) every 3 h from 2011-10-23 12Z (T+60) to 2011-10-24 03Z (T+75).

created heavy precipitation in a double front structure that makes the numerical forecasting of the case even more challenging.

It is beyond the scope of our study to untangle the dynamical mechanisms and all the details behind the above described developments. There are large scale drivers, such as the divergence aloft associated to an upper level jet exit region, enhancing low level convergence to trigger the initial stages of cyclogenesis in both the first and second frontal wave developments (Figure 5). It is also likely that diabatic processes played a significant role in the evolution of the system, since the front had an associated atmospheric river, with nearly saturated conditions in the lower levels. The important issue here is that the interplay between large scale and mesoscale factors in this situation provides a good example for the discussions in the previous sections on the impact of wave selection on spectral nudging and the general behaviour of the solution of the model with this technique.

3.4.2 Spectral nudging results vs. cut-off wave number

Figure 7 shows in each row the 500 hPa geopotential height (contour) and its difference against GDAS (shaded) for experiments with free run, spectral nudging with cut-off wave numbers equivalent to wavelengths of 2000, 1000, 750, 500 and 250 kilometres and grid nudging. Additionally, GDAS fields are plotted in the bottom row as a reference. Each column corresponds to increasing modelling times from T+60 to T+75 hours. The same configuration is used for the remaining Figure 8, Figure 9 and Figure 10. Differences against GDAS are largest in the free run experiment, they are rapidly reduced in

experiments SP2000 and SP1000, and no further reduction is observed with an increase in the cut-off wave number, as discussed in the previous section. The geopotential height at 500 hPa is a relatively smooth field and, as contours show, the differences against GDAS are

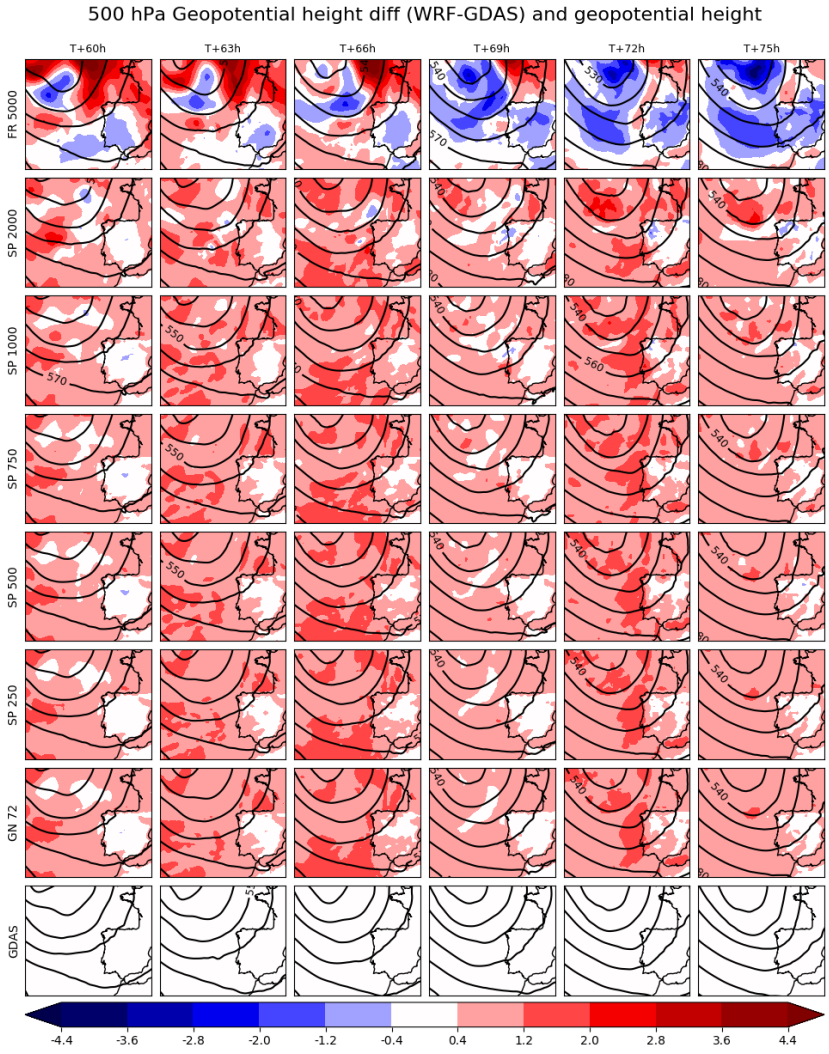

Figure 7: 500 hPa geopotential height (dm, contour) and differences against GDAS (dm, shaded) every 3 h from 2011-10-23 09Z to 2011-10-24 03Z for each WRF experiment and GDAS (rows).

due to shifts in the position of large scale features, and not because of fine scale differences. At the lower 850 hPa level near the top of the boundary layer, the geopotential height (Figure 8, contour) and specially the wet bulb potential temperature (thetaw, Figure 8, shaded)

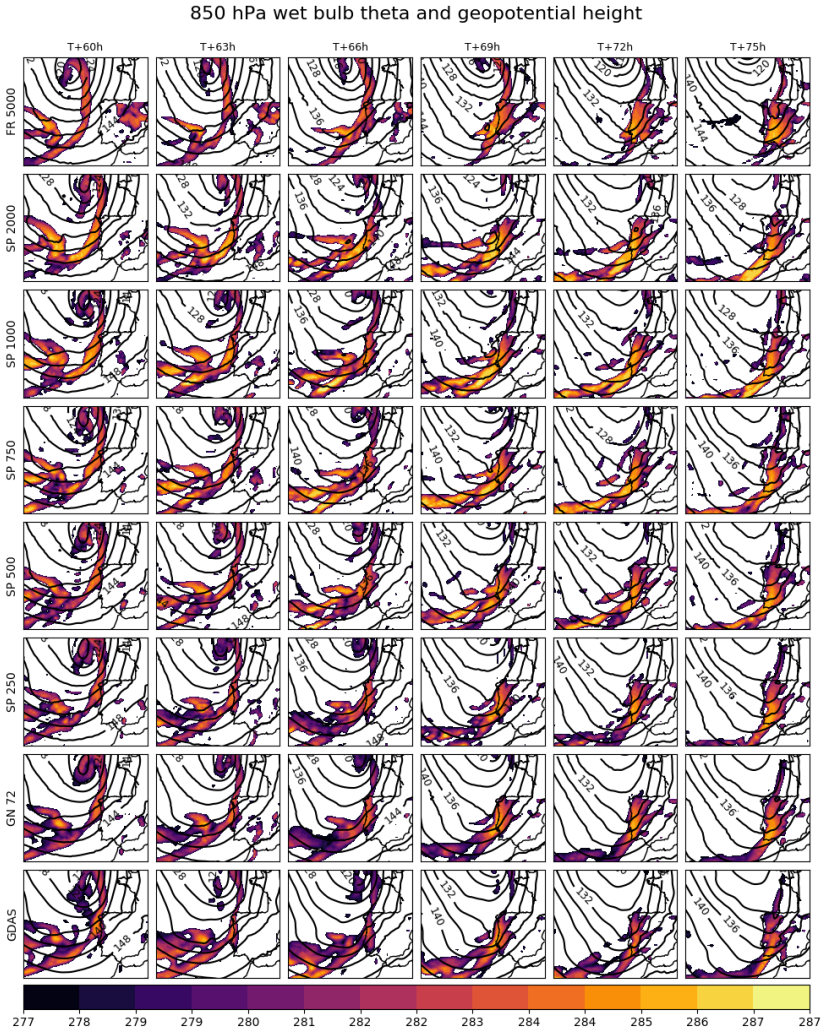

Figure 8: 850 hPa geopotential height (dm, contour) and 850 hPa wet bulb potential temperature (Kelvin, shaded) every 3 h from 2011-10-23 09Z to 2011-10-24 03Z for each WRF experiments and GDAS (rows).

have more small scale structure. Thetaw is shown here as an indicator of the position and complexity of the frontal zones. The intensity of the frontal systems is clearly attenuated as the configuration gets closer to grid nudging, eventually becoming very similar to GDAS. More so,

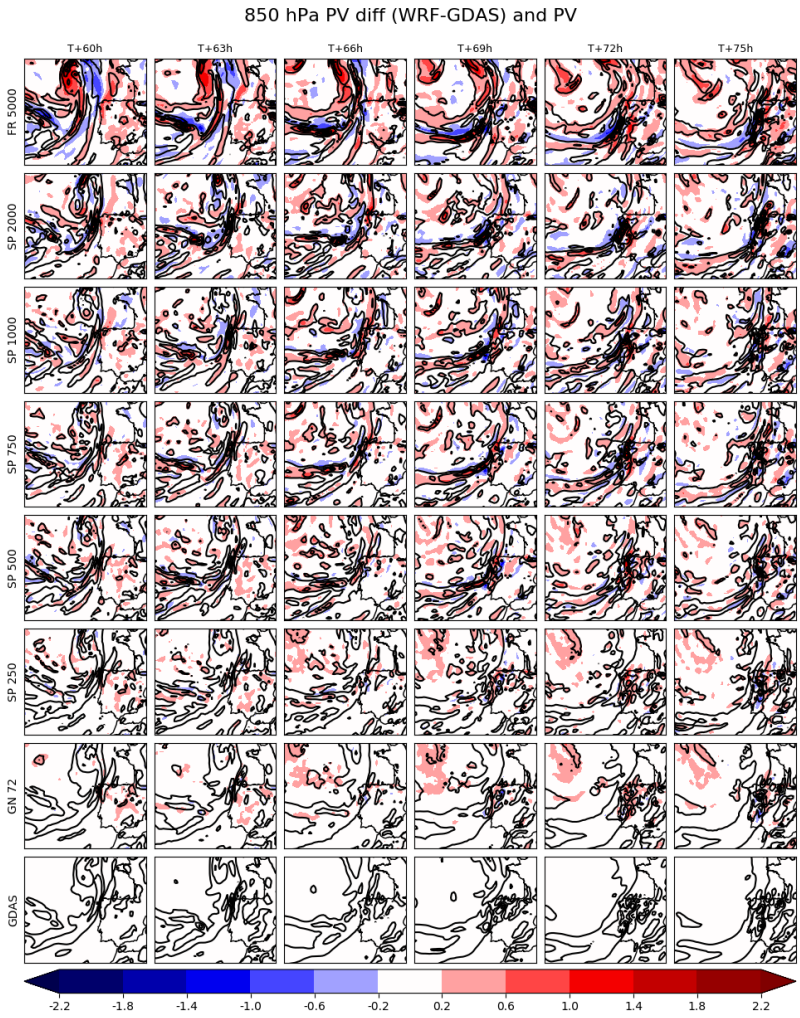

Figure 9: 850 hPa Potential vorticity (pvo units, contour) and its difference against GDAS (pvo units, shaded) every 3 h from 2011-10-23 09Z to 2011-10-24 03Z for each WRF experiments and GDAS (rows).

some finer scale features that are present in SP2000 and SP1000 are damped as the WRF solution approaches GDAS, which is not able to reproduce them. This is the case of the secondary front located behind the principal, at T+66, that appears to be fully developed for

Figure 10: MSLP (hPa, contour) and 3 h accumulated precipitation (mm, solid) every 3 h from 1200 UTC 23 October 2011 to 0300 UTC 24 October 2011 for each WRF experiments and GDAS (rows).

experiments with solely waves longer than 1000 km wavelength nudged, as in SP1000, and it is progressively less intense when shorter waves are nudged, until it becomes non-existent for GN.

Figure 9, depicting the 850 hPa potential vorticity (contours) and the differences with GDAS (shades), shows that the fine scale features produced by WRF, absent in the GDAS solution, are not only localised at the frontal area, but they are spread all over the domain. For experiments FR and SP2000, the differences represent mostly a displacement in the large scale field; a shift in the front position revealed by the existence of alternating positive and negative differences. For SP750 and smaller nudging wavelengths, there are still some small misplacement errors in the front's position, but the differences mostly represent areas where the WRF solution has higher PV than GDAS. This is particularly true in the Atlantic NW of the Iberia Peninsula, where high PV is associated with a more intense cyclone in WRF than in GDAS. In general, the difference fields suggest that the solution from WRF contains many more small scale features than present in GDAS, which, as the cut-off wave number increases, are damped resulting in a solution for SP250 and GN that contains large scale patterns only, similarly to GDAS.

Finally, Figure 10 shows the 3 hour accumulated precipitation (shaded) together with mean sea level pressure (contour). Experiments SP2000, SP1000 and SP750 produce an identifiable round precipitation structure at T+66 and T+69, which is also observed in TRMM (Figure 6), although the precipitation amount seems unrealistically high for SP2000. This secondary structure is responsible for the precipitation in the North West of the Iberian Peninsula at T+72 and T+75, whereas the primary front is responsible for the precipitation in the Centre/South-West. The Atlantic coastal area of the Iberian Peninsula has a complex terrain that plays a big role in defining the structure of the precipitation and we do not expect our modelling set-up to be able to represent the fine spatial variability of the rain. Nevertheless, experiments SP2000, SP1000 and SP750 are able to reproduce the two precipitation areas remarkably well, given the low resolution of the simulation. As we move to higher cut-off wave numbers, the secondary structure becomes

less identifiable and the two distinct precipitation areas in the Iberian Peninsula collapse into one, caused by the primary front. The same behaviour is observed in the FR experiment.

It is also noteworthy to remark that some experiments produce high precipitation areas that are not present in the observations. The FR experiment generates high precipitation at T+66 and T+69 in the eastern Iberian Peninsula and experiments SP250 and GN72 have a slightly more intense precipitation than others at T+60 in the North West of the Iberian Peninsula, corresponding to the high precipitation area at the same location seen in GDAS. None of these are present in TRMM, neither in the experiments with lower cut-off wave numbers, suggesting that spectral nudging is not only improving the forecast of the main synoptic feature but also removing spurious precipitation elsewhere, that is, it is modifying the solution in the whole domain.

3.5 SUMMARY AND CONCLUSIONS

Spectral nudging is a well-established technique in numerical modelling that has been implemented in various applications, from NWP to regional climate downscaling. Although many publications have explored a variety of different aspects of the method, not many have studied in detail the impact of two key parameters of the technique on the model solution: i) the cut-off wavenumber that separates the scales where the nudging is applied from those where the model evolves freely and ii) the spin-up time that is required for the model to reach a balance between the nudging effect and the development of its own features. The first parameter is crucial in any spectral nudging application, whereas the second one becomes particularly relevant in single case studies, where simulations are generally initialised from coarse resolution analyses, and the LAM needs some spin-up time before it generates small scale structures.

Our modelling set-up consists of a limited area model covering the South West of Europe, with a substantial part over the ocean to include the synoptic systems that typically affect this region. Three one-month periods, representing typical summer, winter and in-between conditions, were selected and suites of different experiments where the

spectral nudging cut-off wave number was changed were performed daily with a 96 h duration. Additionally a grid nudging simulation and a free run (no nudging) were also performed as reference. We focused our study on comparing the solution of the LAM with the boundary condition data, which is also used as the reference field for nudging.

When using spectral nudging, the RMSD against lead-time stabilizes after 36/48 hours from initialisation, with a more random behaviour earlier in the runs. This is a longer spin-up time than for grid nudging and shorter than for the free run experiment. Even though the strength of the nudging, as given by the relaxation timescale, is the same in all experiments with nudging, the constraint on the model solution is strongest in grid nudging because the entire spectrum is forced, and amplitudes of the components are damped even when there is not any in the analysis for the same wavelength. For this reason, the model reaches a balance between the nudging constraint and its own climate much more rapidly than in spectral nudging, where a part of the solution is still unconstrained. The free run experiment, with no internal forcing at all, requires the longest spin-up time, exceeding the 96 h duration of the simulations.

The spectral structure of the analysed variables shows that spectral nudging is able to alter the longer wave spectral modes below the cut-off wave number to make them equivalent to those in the boundary condition. The shorter wave modes above the cut-off wave number maintain meanwhile the same magnitude as in the simulations without nudging. This suggests that, with spectral nudging, the divergence between the LAM and its boundary condition is due to the development of high frequency features not present in the coarser boundary condition data. For this reason, the RMSD of the model against the boundary condition is larger for the experiments with smaller cut-off wave numbers, and the higher the cut-off wave number, the more similar the model solution is to GDAS. The free run has the largest RMSD and the experiment with Grid nudging the smallest, with the different spectral nudging cases lying in between. When experiments are performed with weaker nudging coefficients of 3 h^{-1} and 6 h^{-1}, grid nudging is able to generate more high frequency information at the end of the spectrum.

However, these small-scale components in GN never reach the amplitude seen in spectral nudging experiments with the same nudging coefficient. In fact, when a low cut-off wave number is used, spectral nudging produces comparable high frequency amplitude to free run. This gives confidence in the generality of our results and supports the idea that spectral nudging is much more efficient in allowing the LAM to generate the same high frequency information as it otherwise would, should nudging were not applied.

The behaviour of the RMSD against the cut-off wave number clearly shows that the error decreases very rapidly as the cut-off wave number increases, and that most of the reduction in the error is gained from the nudging of the larger scales. For values exceeding a certain cut-off wave number, the RMSD barely changes any longer, and its minor variations can be explained by the damping of the small-scale structures generated by the LAM. We have estimated the inflexion point in the RMSD trend to be close to the 1000 km length scale, and this value is consistent in the vertical for all levels up to 10 km.

A physical explanation for the latter result is that the 1000 km scale corresponds to the Rossby Radius of Deformation, which is commonly interpreted as the scale where rotational effects become less important when compared with buoyancy, setting the transition from the synoptic scale to the convective scale. By selecting a cut-off wave number in the range of 1000 km wavelength, we are effectively nudging the synoptic scale in the model solution to the analysis, while still allowing the model to develop its own finer scale contribution. The example case used in our study shows that the simulations with a nudging scale close to the Rossby Radius yield the most realistic results, similarly to what other studies have found (Liu et al., 2012; Wang and Kotamarthi, 2013).

The closest wave number to a given R length scale can be found with the expression:

$$n = \frac{D_{x,y} N_{x,y}}{R} + 1 \qquad (6)$$

where *n* represents the wave number in the x/y-direction, $D_{x,y}$ is the resolution in the x/y-direction, $N_{x,y}$ is the number of gridpoints on the x/y-direction and *R* is the Rossby Radius, taken to be 1000 km. The unity value added in *(6)* accounts for the fact that the WRF spectral nudging implementation considers the first term of the FFT (wave number zero) as *n=1*. For our particular model set-up, this expression results in $n_x=5.2$ and $n_y=4.7$, which after rounding up to the nearest integer, yields the values used in the experiment (SP1000) that best matched the observations.

4 The impact of wave number selection and spin-up time in tropical latitudes

4.1 INTRODUCTION

In the previous chapter, we found that the optimal values of the spin- up time and cut-off wave number can be derived from the synoptic behaviour of the area that is being modelled. Although our conclusions aimed to be generic, the question still stands if the derivation can be applied to other areas of the planet; particularly in the Tropics, where the synoptic systems have very different dynamics to those in the mid-latitudes. In order to confirm our hypothesis, it is critical that the nudging scale should be related to the typical scale of the synoptic systems (i.e. Rossby Radius of Deformation) and not with other factors related to the experimental set-up such as the resolution of the forcing dataset or the model resolution. To ensure that our study is comparable with the one from Chapter 3 we follow a similar experimental methodology and analysis.

This chapter is organized as follows. In Section 4.2 we describe the experiments. In Section 4.3 we present a statistical analysis of the results and in Section 4.4 we test the validity of our findings in different hurricane cases. Finally, in Section 4.5 we summarize our findings.

4.2 EXPERIMENTAL SET-UP

4.2.1 Model description and configuration

For this work we use version 3.5 of the Advanced Research WRF (ARW) modelling system (Skamarock and Klemp, 2008), set up with a single domain centred over the Dominican Republic. The domain covers an area from the equator to mid latitudes and has 400x300 horizontal points at 20 km resolution and 33 vertical levels (Figure 11). This domain is design to hold the trajectories of most hurricanes occurring in the area. Model initialisation and forcing is provided by NCEP Global Atmospheric Analysis (GDAS) at 3 hour frequency and the physical configuration of the system is described in Table 3.

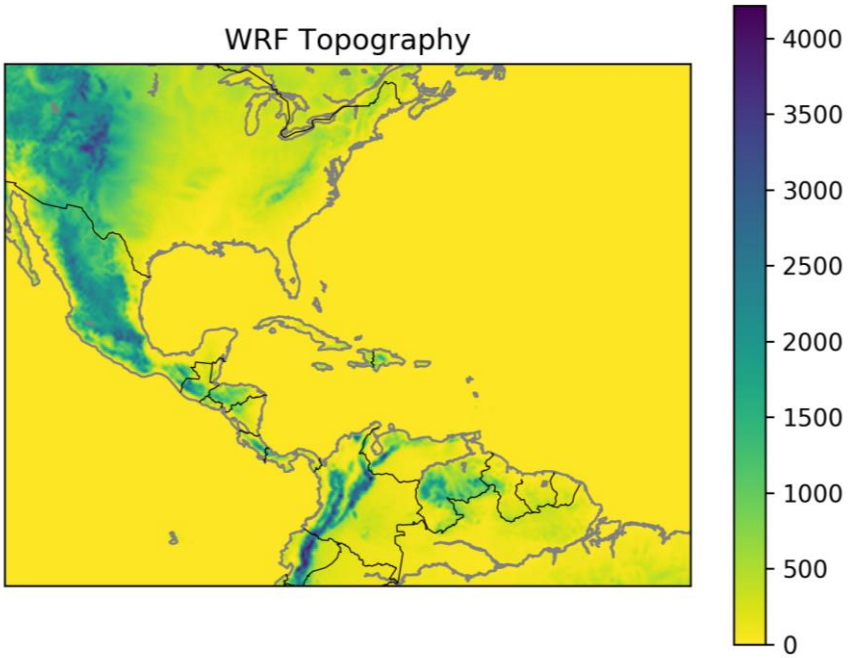

Figure 11: Model topography (meters) for the domain used in all experiments from Chapter 4.

In experiments with nudging, this is applied to temperature, humidity and wind. As in Chapter 3, we choose to nudge wind in the full atmospheric column, while for temperature and humidity nudging starts to be applied from level 10 to 15 gradually, and then at full strength above this level (see Section 3.2.1 for the justification of this approach). This varies slightly from the methodology used in Chapter

Parameterisation	Scheme	Reference
Micro-physics	WRF Single Moment 6-class	(Hong and Lim, 2006)
Long wave radiation	RRTM	(Mlawer et al., 1997)
Short wave radiation	Dudhia	(Dudhia, 1989)
Surface layer	MM5 similarity	(Skamarock et al., 2008)
Land surface	5-layer thermal diffusion	(Skamarock et al., 2008)
PBL	Yonsei University	(Hong et al., 2006)
Cumulus	Kain-Fritsch	(Kain, 2004)

Table 3: Physic parameterisations used in the WRF modelling set-up

3, where we choose to nudge temperature and humidity above the WRF estimation for the PBL, instead of at a fixed level. While our tests suggest that there is not much difference between the two methodologies, the WRF PBL estimation varies substantially horizontally, even across the same synoptic system (i.e. along a cold front). Nudging above a fixed model level ensures that the same nudging force is applied along the domain regardless of the particular synoptic situation. The nudging coefficient is set to $3 \cdot 10^{-4}$ s^{-1}, which is the same value used in the previous chapter.

4.2.2 Experiment description

For our experiments, we select 6 periods from the years 2010 to 2015, all starting on the 21st August and ending on the 21st of September of each year. The hurricane seasons from 2010 to 2012 are some of the most active in recorded history, both in named storms and damage produced; while the seasons from 2013 to 2015 were below average in terms of hurricane production. This ensures that our simulations are representative of a wide variety of situations in the area and the extended number of cases gives statistical robustness to our results. Hurricane activity typically peaks in mid-September (Landsea, 1993).

Exp	Nudging	WN_X	WN_Y	Length X	Length Y
FR 8000	Free run	No Spectrum		8000	6000
SP 4000	Spectral	3	3	4000	3000
SP 2000	Spectral	5	4	2000	2000
SP 1600	Spectral	6	5	1600	1500
SP 1300	Spectral	7	6	1333	1200
SP 1000	Spectral	9	7	1000	1000
SP 700	Spectral	12	9	727	750
SP 500	Spectral	17	13	500	500
SP 375	Spectral	22	17	381	375
SP 250	Spectral	33	25	250	250
SP 125	Spectral	65	49	125	125
GR 75	Grid	Full Spectrum		40	40

Table 4: Nudging configuration for each experiment. Wave numbers correspond to a Fourier series where 1 represents the non-oscillatory term of the FFT. This follows the criteria used in the WRF implementation. Experiment SP 1300 was only used for the hurricane cases.

For these particular years, starting from the last week of August to the end of September allows the inclusion of a significant number of major hurricanes in the simulations.

In our simulations we run 12 nudging configurations. Ten of these are spectral nudging experiments using different cut-off values equivalent to spatial scales from 4000 km to 125 km. Another configuration uses grid nudging and the last one uses no nudging at all, which we refer to as *free run* (Table 4). Each one of the 11 configurations is run for 4 days starting at 00Z every day of each month of the 2010-2015 period, which adds to 1800 model simulations. Each experiment starting on the same day shares the same initial and boundary conditions so each difference in their solution is due to the changes in the nudging set-up. The values in the cut-off wave number shown in Table 4 are selected to have approximately the same length in both horizontal directions. The experiments are tagged with the length scale of the X direction. Free run and grid nudging experiments are given a characteristic nudging length scale which corresponds, respectively, to the full domain and 2 times the model resolution (smallest possible wavelength). Results from this chapter and Chapter 3 show that is acceptable to consider these configurations as asymptotic cases of spectral nudging.

4.3 RESULTS

To make this study fully comparable with the results in Chapter 3, the evaluation methodology applied to the results of our simulations follows very closely what has been described in Section 3.3. For this reason we present a shorter description of the methodology here. A full discussion on the steps followed can be found in that previous section.

The results from our experiments are compared to NCEP Global Data Assimilation Analysis (GDAS), which is our driving dataset and allows to understand how the model diverges from its boundary condition, and to ECMWF ERA-interim reanalyses, which represents an independent verifying truth. The fields from both datasets are interpolated to the WRF model grid, horizontally and vertically, and we perform the comparisons at different model levels. Scores are

calculated for all nudging variables: potential temperature, specific humidity and wind components (which are presented as kinetic energy for convenience). To avoid redundancy in our plots, unless noted, only kinetic energy is presented as results are comparable for the other variables. Since all 1-months periods correspond to the same time of the year, all the simulations from 2010 to 2015 are included in the calculation to increase the statistical robustness.

4.3.1 Power Spectrum and RMSD

We conduct the same analysis as in 3.3.1 and 3.3.2 to investigate the impact of spectral nudging in the solution of the WRF model; full explanation of the methodology can be found in those sections. We include all the experiments for the 2010-2015 period in the evaluation as they are all from the same hurricane season. Also, we present results for the X-direction (when applicable) and wind kinetic energy as results are comparable for Y-direction and other variables.

We depict the power spectrum for each configuration at three different levels in Figure 12 (inset panels). In general, all experiments show the same behaviour at the larger scales, indicating that their synoptic setting contains similar information. As lines move towards the smaller scales, the different nudging configurations start to show different behaviours. This reveals the impact of changing the spectral cut-off wave number, where the experiments start to diverge from each other as they move to shorter wavelengths. The relative difference against GDAS (Figure 12, main panels) reveals how the spectral structure of the WRF solution is changed with respect to its forcing, where grid nudging and free run represent the asymptotic behaviours. On one hand, grid nudging is similar to GDAS at all scales, showing only some divergence with its boundary condition at the smaller scales, on the other hand, free run shows similar values to GDAS only at larger scales, but soon separates indicating that is able to generate more complex small scale behaviour. Spectral nudging cases show an intermediate behaviour where they have a similar value to grid nudging below the cut-off wave number and they recover the free run behaviour afterwards. At higher levels, all experiments are closer to the GDAS large scale than that at lower levels. This reflects the fact that the

atmospheric fields at this height are smoother (i.e. less turbulent) than in the lower troposphere. At the 5000 m and 1200 m heights, all experiments show differences with GDAS in the kinetic energy spectra even at the larger scales, indicating that they produced different results

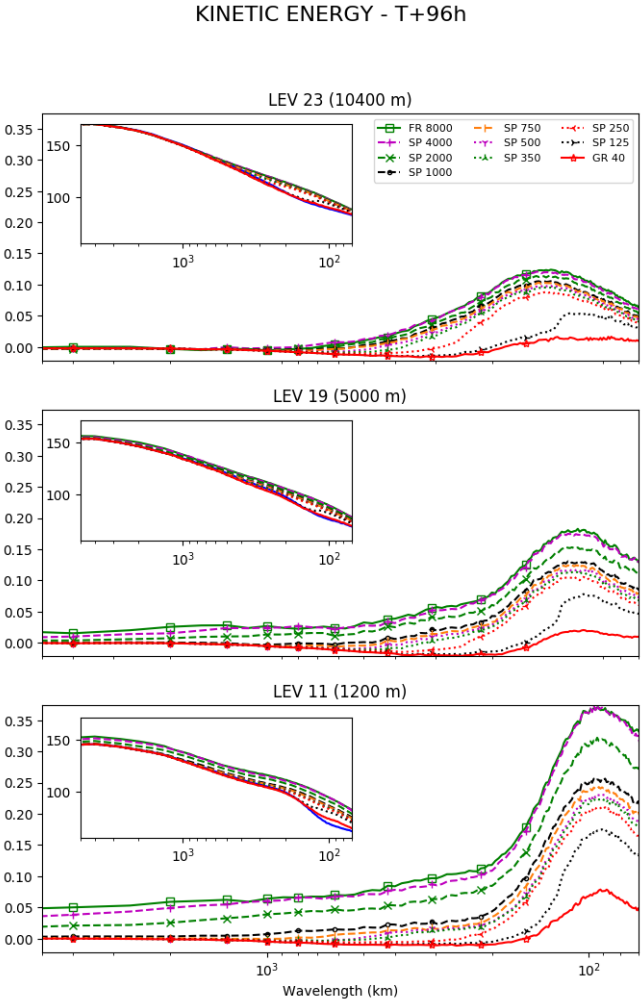

Figure 12: Kinetic energy power spectra (db) for all experiments (inset panels) and their fractional differences against GDAS at modelling lead time 96 h (main) for model sigma levels 11, 19 and 23. Results correspond to all simulations run between 21st of August to 21st of September from years 2010 to 2015.

not only in the short scale but also in the synoptic scale. This is a consequence of experiments with free run and spectral nudging with lower cut-off wavenumber diverging from GDAS developing unrealistic low pressure systems in the interior of the domain. In Section 4.4.2 we present a more complete discussion, and in Figure 16 we show an example of this.

RMSD against GDAS and ERA-interim (Figure 13) shows that free run and grid nudging have the larger and smaller values, respectively, which is in agreement with the results from the previous paragraph. Free run RSMD grows at a steady rate as the lead time advances. This reflects the fact that the model is developing its own solution in the interior of the domain; this is a consequence of being driven only at the boundaries, with no extra forcing applied in the interior of the domain. Applying spectral nudging, even at the smallest wave number, has an immediate constraining effect, preventing the model from separating from its boundary condition. As larger wave numbers are used, the model becomes more similar to GDAS and ERA-interim, and it needs a shorter time to reach a steady behaviour. Ultimately, grid nudging reaches a steady value in the shortest time, which indicates that this experiment, and spectral nudging experiments with the highest wavenumbers, are very close to GDAS and ERA-interim and they are not developing their own independent solutions.

The analysis of the Power Spectrum indicates that spectral nudging is very effective at separating the nudged scales from the ones that are not nudged. The non-nudged scales develop a similar size to the free run case, while the nudged scales are closer to the grid nudging case. Similar to what it was observed at mid-latitudes, applying large cut-off wavenumbers (i.e. nudging smaller scales) results in the removal of critical small-scale information. Conversely, the experiments with the largest cut-off wavenumber have the lowest RMSD, but this is due to the fact that GDAS and ERA-interim have a fairly low resolution and the experiments with less short scale information (i.e. smoother fields) verify better against them. It can be seen that nudging in the largest wavelength represents a substantial improvement in the model solution, due to a better representation of the larger scales (i.e. synoptic

situation), however nudging in the shorter scales makes the model more similar to GDAS and ERA-interim and prevents it from generating finer scale features, which is undesirable. Therefore, the most appropriate wavenumber should be large enough to prevent WRF from drifting

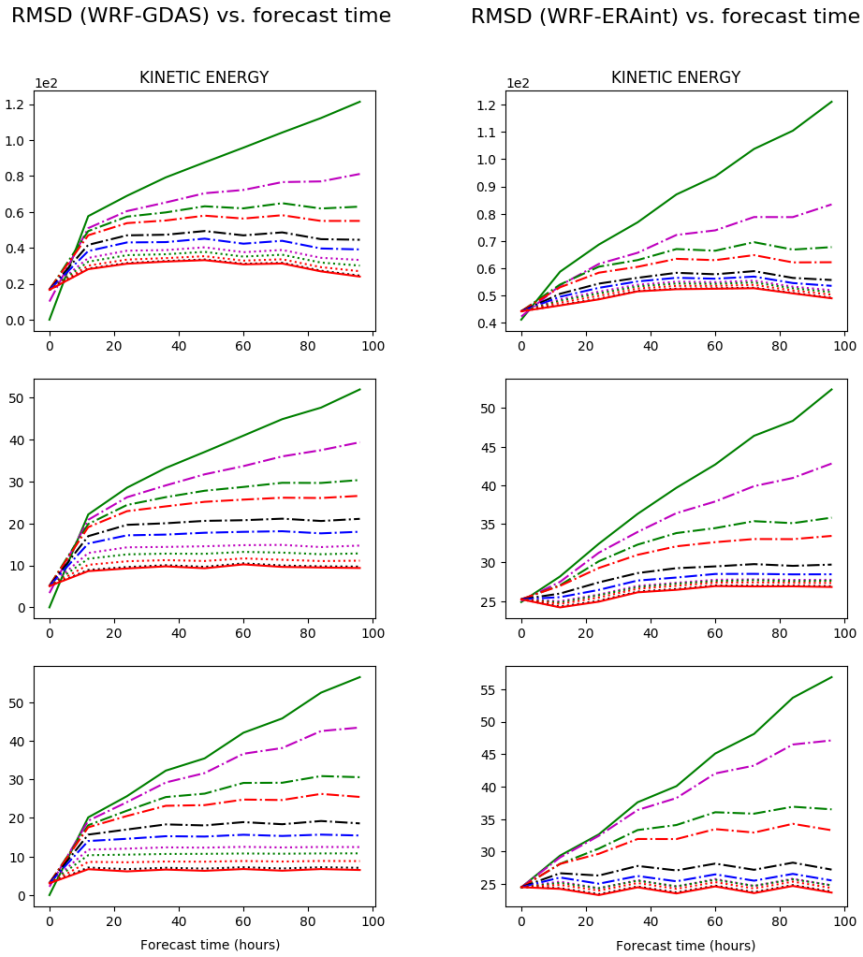

Figure 13: Root mean square distance between WRF and GDAS (left) and between WRF and Era interim (right) versus forecast time for kinetic energy (J). Results correspond to all simulations run between 21st of August to 21st of September from years 2010 to 2015 and model sigma levels 11, 19 and 23. Colours and symbols of the curves are as in Figure 12.

from its boundary condition, but not so high that it does not allow it to develop its internal high resolution dynamics.

4.3.2 RMSD vs Cut-off wave number

In Figure 14 (a, c) we plot the RMSD against the cut-off wavelength of each experiment for three model levels at 96 h lead time, when most experiments seem to have passed the spin-up phase (see previous chapter for justification of this). Free run and grid nudging are also included as asymptotic cases, and although they do not have a cut-off wavelength, we use the domain size and two times the model resolution, respectively, to include them in the graph (Table 4). Results are calculated using all experiments from 2010 to 2015.

Results show that most of the reduction in the RMSD is achieved by nudging the largest scales and, after a certain inflection point, the curves flatten and not much change occurs (Figure 14, a, c). Applying nudging above certain wavelength results in almost no change in the RMSD, and according to the results presented in Section 4.3.1, it would be at the expense of dumping the high spatial frequency contribution from WRF. This is in agreement with what was observed in the mid-latitude experiments and the same conclusion applies here: the cut-off wave number should be selected so that a significant part of the error is reduced, but the high frequency information from the LAM is preserved.

In 3.3.3 we used a geometric method to estimate the optimal value of the cut-off wave number which did not consider the physics of the system or the nature of the error. Here we propose an improved methodology that is based on a physical approach. In Jung and Leutbecher (2008) the authors investigated the separate contribution of the planetary, synoptic and sub-synoptic scales to the error of a global ensemble. They estimated that the size of the error was 7 times larger for the synoptic scale than for the mesoscale. In our plots, we indicate (Figure 14, a, c) the point of the curve where the RMSD is reduced to a 15% of the range. The points depicted in the figure are reasonable close to the inflection point, which is quite remarkable as the method does not make any assumption on the shape of the curve.

The inflection points for levels between 1000m and 10,000m are plotted in Figure 14 (b, d). Results for the RMSD against GDAS (Figure 14, b) show that kinetic energy and theta inflection points occur around 600 km, slightly lower for specific humidity, and for larger values when they are calculated using the RMSD against ERA-interim (Figure 14, d). The GDAS and WRF share the same large scale fields (the former drives the latter) which implies that they are going to be closer to each other and curves are going to be skewed towards the smaller scales. Since ERA-interim represents an independent, verifying truth, the RMSD against this dataset will be more representative of the error of the model and, therefore, we focus our analysis on these results only. Here the inflection points occur for larger values, at clearly separated scales for each variable and with a remarkable consistency in the vertical. This highlights the barotropic nature of the Tropical latitudes.

The average value for theta, kinetic energy and specific humidity is depicted in the legend of Figure 14 (b, d), showing values around 2000 km for theta, 1100 km for kinetic energy and 750 km for specific humidity. This result differs substantially from Section 3.3.3, where we show the same plots for mid-latitudes and where all variables have similar values around 1000 km. One possible explanation lies in the fundamental differences of the weather systems between the mid-latitude and the tropical systems. In the former, the spatial structure of the three variables is mostly driven by the synoptic setting, where the position of low pressure systems and fronts plays a key role. However, in tropical latitudes, there is a greater variation in scale where, on one hand, temperature is generally smoother and, on the other, humidity varies spatially due to strong and active convection. It is also reasonable to consider that kinetic energy behaviour would lie between the two other variables, having a generally coarse structure occasionally disrupted by the tropical storms crossing the domain. For this reason WRF is able to get most of the reduction of the RMSD against ERA-interim for temperature at larger wavenumber than it does for specific humidity. It is easier to reproduce a smoother field such as temperature than it is a more complex one with a high spatial variation like the humidity.

One of the main conclusions from 3.3.3 is that there is a relationship between the most appropriate cut-off wave number and the

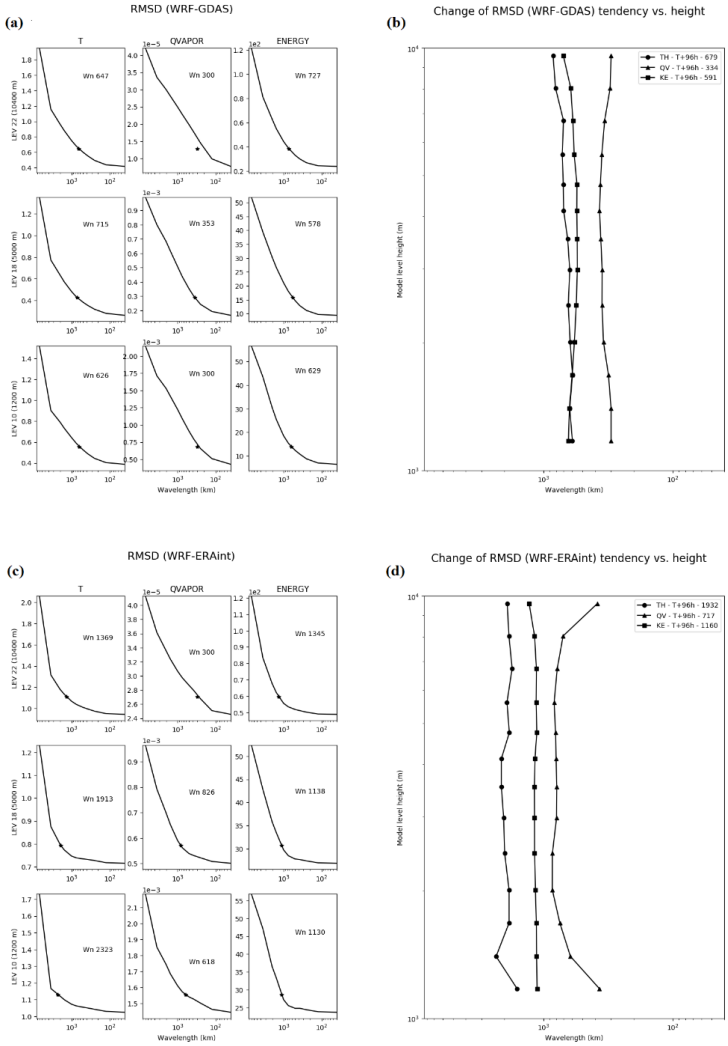

Figure 14: Root mean square distance against WRF-GDAS (a) and WRF-ERA-Int. (c) versus cut-off wavelength. Panels a & c show results theta (Kelvin), specific humidity (kg kg^{-1}) and kinetic energy (J) and for model sigma levels 11, 19 and 23. The WL numbers shown in each plot correspond to the point where the error is reduced to a 15% of its maximum value. Panels b and d depict WL numbers from a and c versus model level for the different variables between the heights of 1 km and 10 km at 96 h forecast lead time.

Rossby Radius of Deformation, which offered a physical interpretation for our results. Near the equator the Coriolis force weakens and we expected the optimal cut-off wave number to correspond to a larger scale for a tropical experimental setting. While none of the studied variables seem to agree with this interpretation at tropical latitudes (i.e. their inflection points occur at very different scales), they do agree if we consider the average value of the optimal inflection points for each variable, which is around 1300 km. This indicates that, on average, our hypothesis still holds and offers further support for our results.

4.4 EXAMPLE CASES

4.4.1 Description of hurricanes

We evaluate our results on 4 hurricanes that occurred between 2010 and 2013 using the same domain (Figure 11), model set-up (Table 3), driving dataset (GDAS) and nudging configuration (Table 4) as in the previous section. In addition, we test a new spectral nudging approach (labelled as 3VARS) where we use different cut-off wave numbers for each nudged variable. This is motivated by our findings from the previous section and we choose them to correspond to 2000 km for temperature, 1100 km for each wind component and 750 km for relative humidity. We added code to WRF to enable us to use a cut-off wavelength, as it is not available in the standard release. The simulations start between 5 and 6 days before the system evolves into a tropical storm. This spin-up time is a bit longer than the 96 hours that we concluded as appropriate in the previous section, but it should be noted that each of the systems studied here evolved from a tropical depression to a tropical storm and, ultimately, became a hurricane. A longer spin-up time is needed to ensure that the system that will eventually generate the hurricane is appropriately defined in the simulation. To verify our results, we use the centre position, pressure and maximum wind from the National Hurricane Center reports (Table 5). The observed tracks of each hurricane can be seen in Figure 15 tagged with the OBS label. The hurricane cases have been selected to represent different trajectory paths representative of typical trajectories in the zone. We briefly describe them here; a comprehensive description of each one of the systems can be found in the appendix 7.1.

- Earl originated in the Tropical Atlantic. It travelled in the zonal direction, bending northwards in the Caribbean and continued moving parallel to the US east coast until it dissipated in Eastern Canada.

- Isaac followed a similar path to Earl in its early stages, but continued traveling westwards, crossing the Gulf of Mexico until it dissipated over the southern US.

- Michael originated in the Atlantic at a relatively high latitude and had a wiggling track that stayed over the Atlantic Ocean throughout its lifespan.

- Ingrid was a short lived hurricane with a trajectory that started and ended in the Gulf of Mexico.

4.4.2 Results

Figure 15 depicts the hurricane tracks forecasted by each one of the experiments for the four hurricane cases alongside the observed positions. In all cases, nudging for nearly any configuration is able to maintain the hurricane close to the observed values while the free run experiment does not prevent any of the hurricanes from drifting to unrealistic tracks. A similar thing happens for SP 4000 for Michael and Ingrid, which can be explained by the fact that their trajectories are developed on a smaller area and applying nudging in the longer scales is not sufficient to prevent them from drifting to an unrealistic evolution. The tracks for Earl and Isaac, which both travelled over a larger area than either Michael or Ingrid, are accurately modelled with all nudging set ups.

System	Category	Season	Dates	Report
Earl	4	2010	25 Aug - 4 Sep	(Cangialosi, 2011)
Isaac	1	2012	21 Aug – 1 Sep	(Berg, 2013)
Michael	3	2012	3 - 11 Sep	(Kimberlain and Zelinsky, 2012)
Ingrid	1	2013	12 – 17 Sep	(Beven II, 2014)

Table 5: Cases of hurricanes and tropical cyclones studied, indicating the category, season, dates and the report from which their position, centre pressure and max wind has been taken.

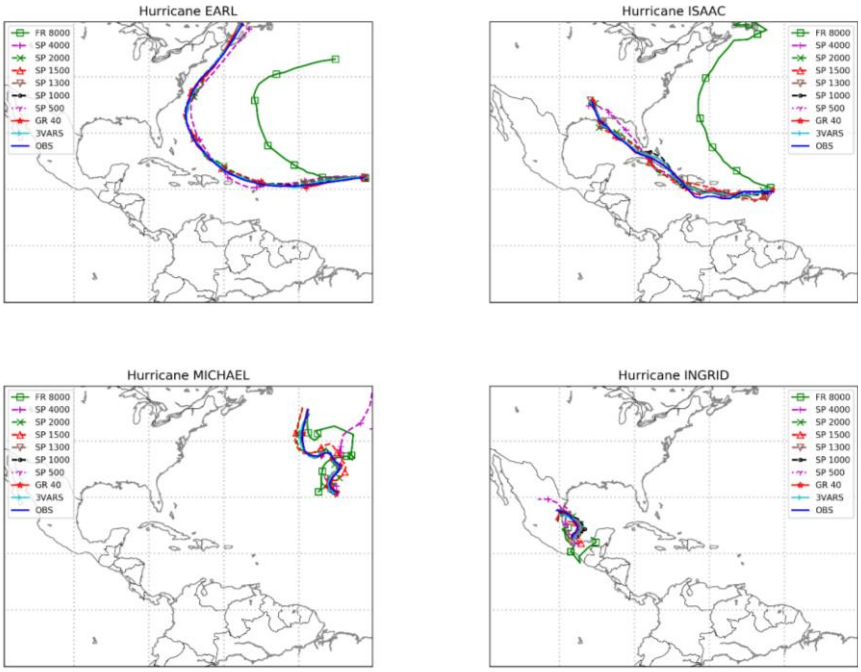

Figure 15: Hurricane tracks for each nudging set-up (see legend) in each panel for the four hurricane cases evaluated in this chapter.

Figure 16 shows maps of mean sea level pressure contours every 4 mb, 24 h accumulated precipitation and centre position for 8 experiments. Fields from ERA5 (MSLP), TRMM (precipitation) and the centre position from NHC reports are also included as verifying truth. Plots represent the fields 5 days after the system turned into a tropical storm and 10 days from the start of the forecast. We choose to show results only for Isaac as comparable results were found for the other hurricane cases.

Similar to our results for mid-latitudes at Section 3.4, the benefits of using an appropriate nudging set-up extends to other parts of the model domain, and not only to the particular area of interest. Consistently with results presented in Sections 3.3, 3.4 and 4.3, experiments with smaller cut-off wave number, FR 8000, SP 4000 and SP 2000 allow to develop more fine scale features than other

experiments. However, in this case, it has a detrimental effect on the solution. This is because many mesoscale cyclones, that are not present in the observations, are simulated by the model forecast. For nudging scales between SP 1500 and SP 1000, the synoptic fields resemble the general structure of the ERA5 and TRMM fields with no presence of the unrealistic structures observed in the experiments with smaller cut-off wave numbers. This is agreement with results shown at Section 3.4 (Figure 9), that suggest that nudging only the larger parts of the spectrum is sufficient to ensure the general synoptic structure is correctly placed. The experiment 3VARS, although it has a fairly large nudging scale for temperature (while not so large for wind and humidity) is able to produce a similar synoptic structure as the one found in the observations, with no trace of the unrealistic cyclones.

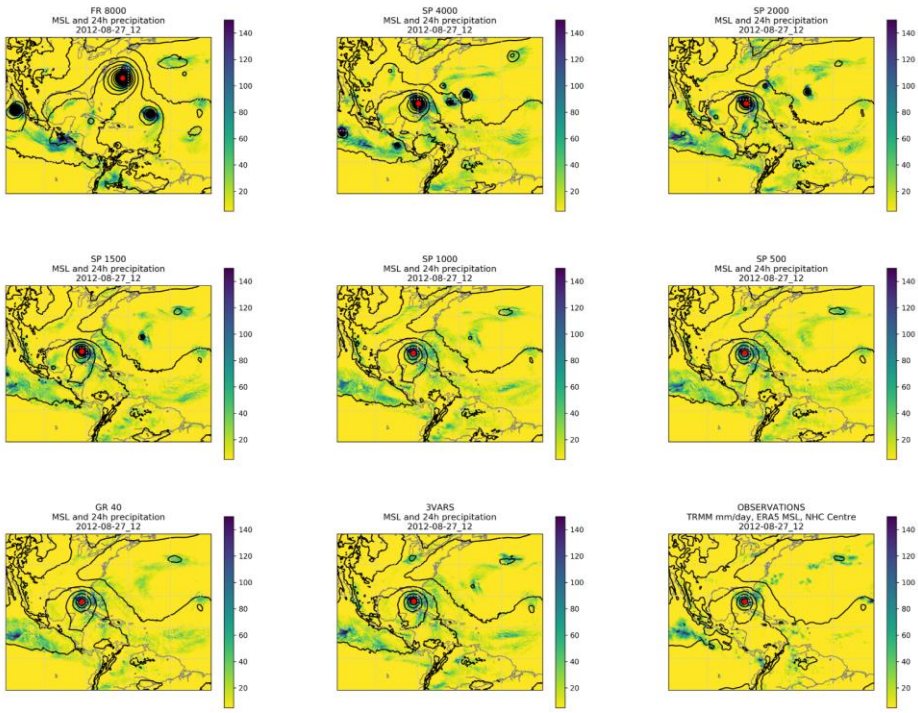

Figure 16: Mean sea level pressure (contours every 4 mb), 24 h accumulated precipitation (mm) (colours) and hurricane centre position (red dot) for 8 different experiments and observations (TRMM for rain, ERA5 for MSLP and NHC report for centre position).

To have a better understanding of how each experiment is performing, in Figure 17 and Figure 18 we show the accumulated error for hurricane centre position or AEPOS (top), centre pressure or AEPRS (middle) and maximum wind or AEWND (bottom) for Earl and Isaac and Michael and Ingrid respectively. The experiments that do not represent the tracks appropriately (i.e. FR, and SP 4000 in Ingrid and Michael) are omitted in the plots as their estimation of the centre pressure and max wind is irrelevant in this context.

The AEPOS shows that, the more parts of the spectrum that are nudged, the better the centre is positioned in the simulation, and that grid nudging and SP 500 consistently perform best in all cases. The two experiments benefit from using the GDAS data assimilation component, which result in these two cases having an accurately positioned centre. However, this is not the case for AEPRS and AEWND where results are more inconsistent for these two experimental settings. In general, experiments with cut off wavenumbers between 2000 km and 1000 km are the best performers. Without considering the 3VARS experiment, for Ingrid and Michael the best result occur in AEPRS for SP1500 and in AEWND for SP1300, and for Isaac and Earl there is not a clear best configuration. Since the optimal cut-off wavenumber depends on the area, and Ingrid and Michael have a trajectory that is constrained in a relatively small one, a particular cut-off wave number setting is able to nudge the optimal large scale features and allows the LAM to develop the local features of the area. It is also noteworthy that Ingrid, which is located further south where the Coriolis force is weaker, performs better with a larger cut-off wave number than Michael. On the other hand, for Isaac and Earl there is not a clear best configuration, reflecting the fact that both systems have a long trajectory that is not localised over a small area. Therefore, there is not a single optimal cut-off wavenumber, as the synoptic structures that interact with the hurricane change in scale as the system moves northwards. Considering the three scores at the same time, the 3VARS experiment is consistently among the best performing

experiments in all variables and hurricane cases, showing the benefits of tuning the cut-off wave number for each variable.

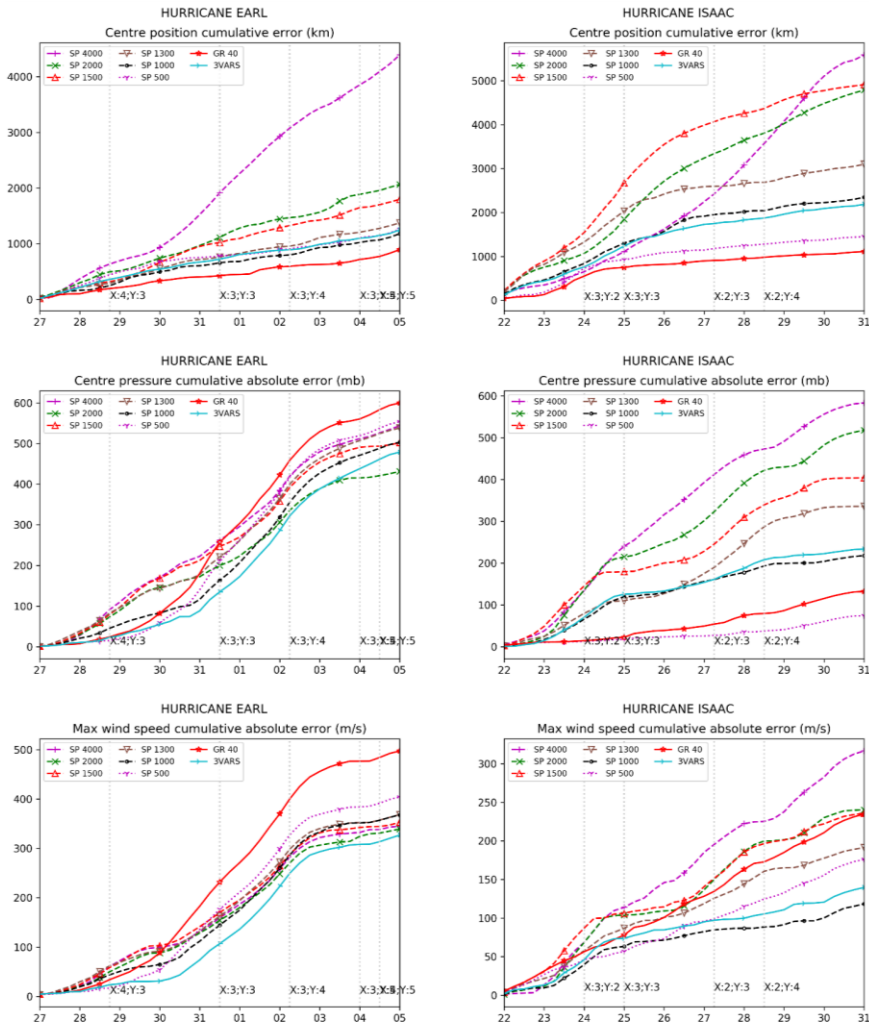

Figure 17: Accumulated absolute error every 6h for centre position (top), centre pressure (middle) and max wind speed (bottom) throughout the hurricane lifespan of Earl (left) and Isaac (right) for each nudging set-up. FR 8000 experiment is omitted in the plots.

The accumulated errors at the end of the evaluation period normalized by the 3VARS case are presented in Figure 19. The variables that have a smaller (larger) error than this case will appear smaller (larger) than 1. Similar to the previous graphs, since FR 8000

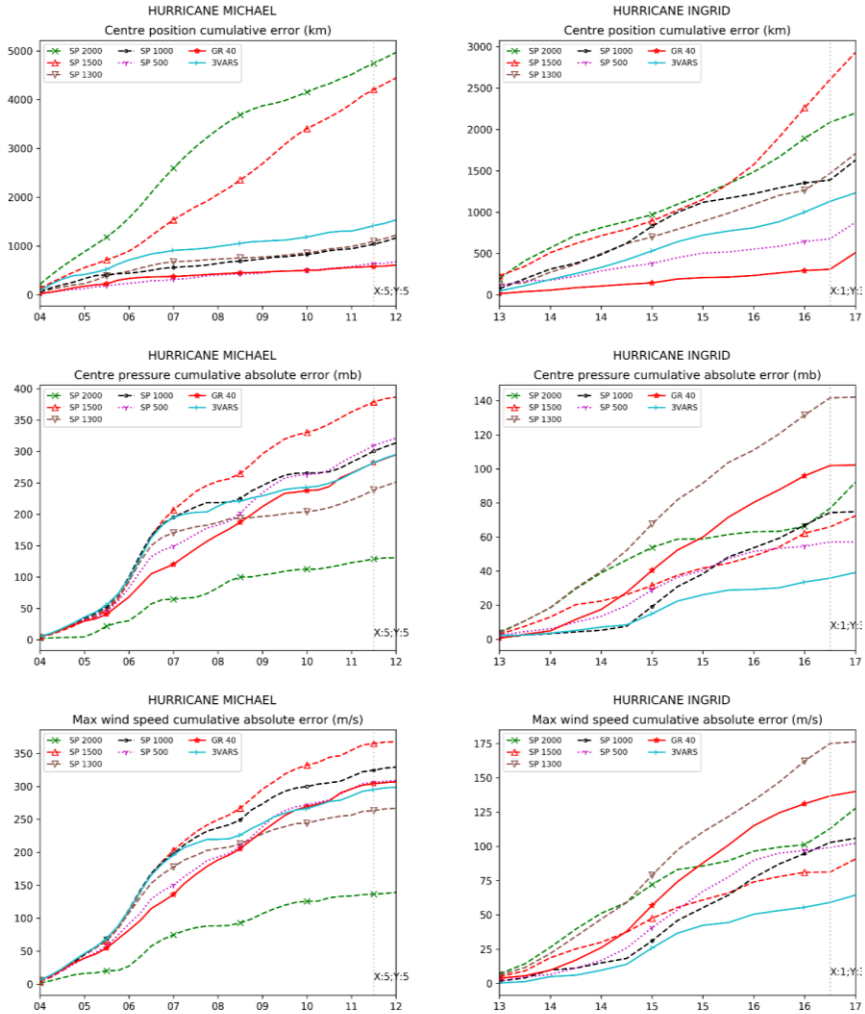

Figure 18: Accumulated absolute error every 6h for centre position (top), centre pressure (middle) and max wind speed (bottom) throughout the hurricane lifespan of Michael (left) and Ingrid (right) for each nudging set-up. Free run case is omitted in the top panels to improve readability. FR 8000 and SP 4000 experiments are omitted in the plots.

and SP 4000 are not able to reproduce the hurricane, are not presented here. The total height of the column in Figure 19 accounts for the accumulated performance across all variables and hurricane cases. This figure summarizes whether a particular case is performing better or worse than 3VARS. The figure confirms that 3VARS setup outperforms the other cases overall, not being the best in each particular variable, but giving a consistently good performance across all the three variables. The only exception is SP 500, which shows a similar performance as 3VARS, but it can be seen that this is largely due to its better accuracy forecasting the centre position of the hurricane (darkest

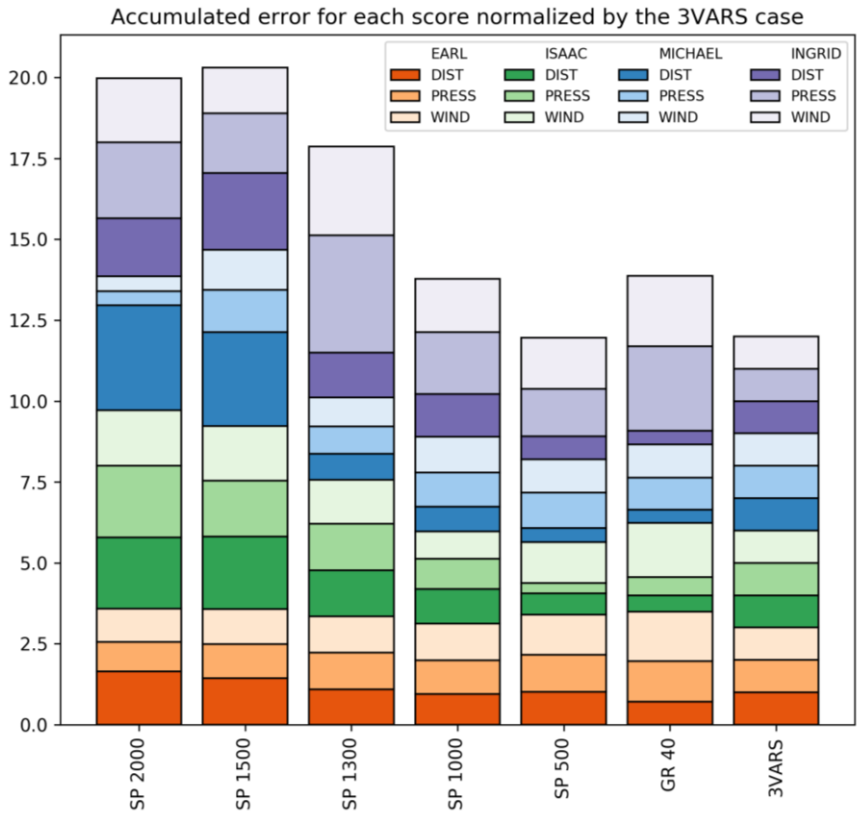

Figure 19: Accumulated error at the end of the evaluation period shown in Figure 17 and Figure 18 normalized by the 3VARS error. FR 8000 and SP 4000 experiments are omitted in the plots.

colours), while having poorer performance in simulating both the centre pressure and maximum winds. This highlights the fact that this experiment, together with GR 40, is able to give a good centre position estimation because is strongly nudged to the GDAS fields, but it fails to develop a hurricane system well enough to deepen the centre pressure and, consequently, to have high enough winds. On the other hand, the 3VARS experiment offers a more balanced prediction of all variables where the centre position estimation is still good compared to most of the experiments and gives a good estimation of the maximum winds and centre pressure.

4.5 SUMMARY AND CONCLUSIONS

The work presented in this chapter is strongly connected to the ideas and concepts introduced in Chapter 3, where we studied the impact of the cut off wave numbers and spin up time in a model simulation using spectral nudging. Our conclusions suggested that the parameter selection is related with the synoptic characteristics of the area and, since the domain was located in a mid-latitude setting, the question remained if the same conclusions were valid at other latitudes, particularly in a tropical setting, which is the objective of this chapter.

For this study, we ran the WRF model over a large domain around the Gulf of Mexico including a substantial portion of the North Atlantic Ocean, where most tropical storms that ultimately become hurricanes are generated. Our modelling set-up is run for 96 h starting every day between late August and late September in the 6 years between 2010 and 2015. This combines the 2010-2012 period, one of the most active hurricane periods in history, with the 2012-2015 period, which was below average, thus, ensuring a wide variety of cases was included in the study. For each day, 12 different configurations were run, including 10 different spectral nudging configurations with varying cut off wave numbers from the lowest to the highest, a grid nudging and a free run setting.

The temporal evolution of the RMSD indicates that the spin-up time, where the model balances with the nudging effect, is found to be between 72 h and 96 h. This spin-up time is double the value found in

the mid-latitudes. It is out of the scope of this work to investigate the reasons why this behaviour is different in the two experimental set-ups and we can only speculate about the subject. It should be noted that the model initial conditions do not contain any water species apart from water vapour, which are set to zero at initialisation. Tropics are typically more covered with clouds than Mid-Latitudes (International Satellite Cloud Climatology Project, n.d.) and, consequently, WRF model needs to develop a larger amount of cloud water from the initialisation closer to the equator than in the poles. The same reasoning can be applied to the other water species (i.e. ice, snow, hail, etc.) explaining why it takes longer to reach a balance with the nudging force in the Tropics than in Mid-Latitudes.

Our analysis of the spectral structure of the model solution reveals that spectral nudging is capable of separating the nudged scales from free running ones, making the model solution similar to the reference fields below the cut-off wavenumber and allowing the model to develop its own dynamics above that wave number. Nudging clearly improves the predictability of the system and applying it at the larger scales allows for the greatest reduction in the error. As nudging is extended to larger parts of the spectrum, little benefit is obtained and it happens at the expense of dampening the higher spatial frequency phenomena in the simulation. This was particularly notable in the hurricane cases presented, where the simulations with the larger cut-off wave numbers underestimated the hurricanes' centre pressure and maximum wind speeds.

Results suggest that the cut-off wave number should be selected so that it provides a significant reduction in the error without dampening the finer scale detail, which is the relevant contribution of the LAM. Our findings suggest that this optimal cut-off wavenumber occurs at different scales for each nudged variable, being 2000 km for temperature, 1100 km for wind and 700 km for humidity. These values are in agreement with each variable's individual synoptic characteristics, accounting for the fact that temperature has a smoother scale structure, humidity is heavily affected by small scale convection and wind lies in between the two. When the cut-off wave number for

each variable is averaged, the resulting value is around 1300 km, which is slightly larger than the Rossby Radius of deformation at mid-latitudes (1000 km). This result is in agreement with the fact that the Coriolis force is weaker near the Equator. This gives further support to our conclusions in Chapter 3 that the optimal cut-off wave number is related to the synoptic characteristics of the modelled area and is not related to any model parameter such as resolution or domain size.

We tested our conclusions in four hurricane cases, where we use the same nudging settings as in the rest of the experiments. Results show that applying spectral nudging even for the larger scales permits an accurate forecast of the track, indicating that the general synoptic situation is crucial to accurately reproduce the position of the hurricane. However, the best forecast of the intensity of the hurricane, which we measure through wind speed and central pressure, is obtained when nudging is applied between 1000 km and 1500 km. This confirms our findings, described in the paragraph above, that suggest that the cut-off wave number should be around 1300 km, and highlights the fact that nudging needs to be applied to the appropriate wavelengths to produce the optimal results. Between the indicated values, there is not a clear optimal value and it slightly changes for each hurricane. We speculate that this could be related with the latitudes in which the hurricane track is occurring, but the number of cases is not big enough and other factors such as the intensity of the hurricane might play a relevant role.

Finally, we introduce a novel approach where we use different cut-off wave numbers for each nudged variable. This configuration performs consistently better than the other spectral nudging set-ups for the 4 evaluated hurricane cases. . This suggests that this new approach might allow to have more flexible nudging configurations that depends less on the latitude or the nature of the modelled phenomena.

5 Spectral nudging as a model initialisation technique

5.1 INTRODUCTION

Spectral nudging is commonly considered a dynamic downscaling technique where the information from the larger scale fields is blended with the solution of the equations of a limited area model (LAM). In nearly all applications, spectral nudging is active through all the simulation ensuring that the synoptic structure is provided at all times by a reference field while the LAM provides the fine-scale details. In this chapter we explore a different approach where we use the technique to initialise the model simulation as a *poor man´s* data assimilation strategy. In this context, the model simulation has two distinct parts: an assimilation window, where the information from observations is ingested into the model fields, and a forecast step, where the model runs benefiting from the improvement in the initial conditions. In our implementation, nudging is activate through a spin-up window (i.e. the assimilation window) and it is disconnected for the rest of the model simulation (i.e. the forecast step).

This approach is not entirely new, as nudging has been used for data assimilation applications in numerous examples that span from the academic to operational NWP in national weather centres such as the Met Office (UK National Meteorological Service) or the Deutsche Wetterdienst (German National Weather Service). References to these various works can be found in Section 1.1. In nearly all of these cases, the model is nudged towards a set of observational datasets that observe limited parts of the full atmosphere. In this work, instead of using a limited set of observations, we study the benefit of nudging our model towards a global analysis where a large set of observations has already been ingested via a complex data assimilation algorithm.

This chapter is organized as follows. In Section 5.2 we describe the experiments and in Section 5.3 we present a statistical analysis. In Section 5.4 we test the validity of our findings using a case study of a

convective episode in the Adriatic Sea. Finally, in Section 5.5 we summarize our findings.

5.2 EXPERIMENTAL SET-UP

5.2.1 Model description and configuration

For our experiments we use WRF ARW version 3.5 (Skamarock and Klemp, 2008) with the same scientific configuration as in previous chapters. See Table 6 for a list of the most relevant parameterizations. The modelling domain covers an extensive area including Europe and North Africa with 272x214 grid points and 32 vertical levels in a rotated pole projection with approximately 24.5 km resolution (Figure 20). This domain has been chosen so that the grid points match exactly the grid of the E-OBS dataset (Van Den Besselaar et al., 2011; Haylock et al., 2008) that is used for verification. Initial and boundary conditions

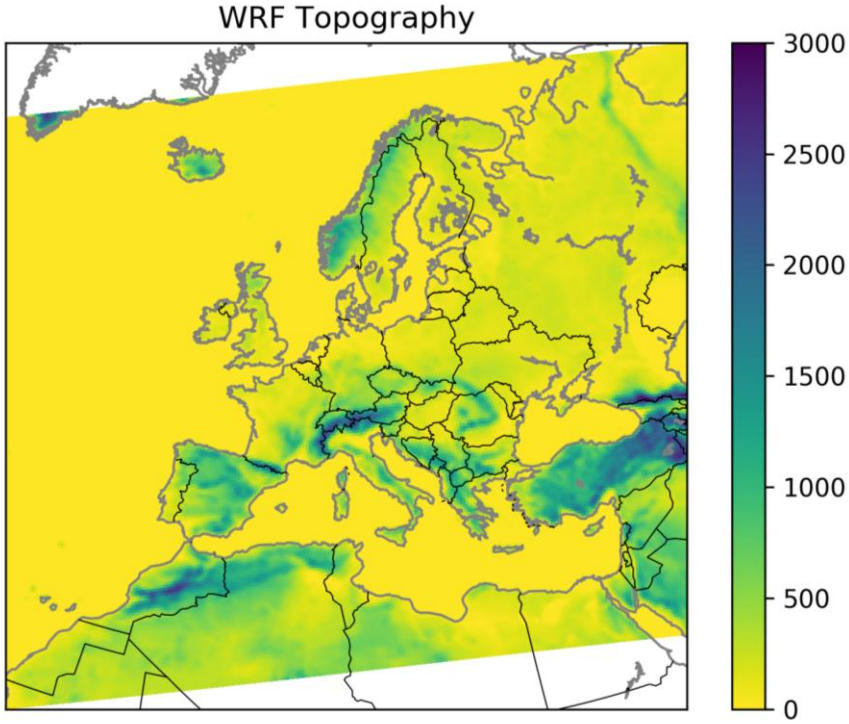

Figure 20: Model topography, the tilted appearance is due to our plotting software not being able to fully handle rotated pole projections.

are provided by the Global Data Assimilation System (GDAS) from NCEP every 3 hours.

We apply nudging to temperature, humidity and wind, with different treatment in the vertical depending on the variable. Both temperature and humidity are nudged starting at level 10 and the strength of the nudging is gradually increased moving upwards to level 15 (approximately 1500 m from model surface) where full nudging is applied up to the top of the model. Wind is nudged on all the vertical levels (see Sections 3.2.1 and 4.2.1 for a justification of this). The nudging coefficient is set to $3 \cdot 10^{-4}$ s^{-1}, which is the same value used for all experiments in this work.

5.2.2 Experiments

We select 3 evaluation periods that cover different seasons in the area of our domain: July 2010, October 2011 and January 2013. According to NCEP global climate reports, these represent a mixture of positive and negative anomalies in temperature and precipitation depending on the area of the domain. The only exception is July 2010, that had a clear positive temperature anomaly across Europe. This ensures that the three periods will be representative of a wide variety of typical synoptic situations in the area.

To evaluate the suitability of spectral nudging as a *poor man's* data assimilation technique we follow a methodology that resembles the typical data assimilation approach in operational NWP centres. When setting up our experiments, we identify two parts of the model run: i) *a spin-up period*, similar to a *data assimilation window*, where nudging

Parameterisation	Scheme	Reference
Micro-physics	WRF Single Moment 6-class	(Hong and Lim, 2006)
Long wave radiation	RRTM	(Mlawer et al., 1997)
Short wave radiation	Dudhia	(Dudhia, 1989)
Surface layer	MM5 similarity	(Skamarock et al., 2008)
Land surface	5-layer thermal diffusion	(Skamarock et al., 2008)
PBL	Yonsei University	(Hong et al., 2006)
Cumulus	Kain-Fritsch	(Kain, 2004)

Table 6: Physics parameterisations used in the WRF modelling set-up

is actively ingesting the larger scale field into the forecast, and ii) a *forecast step*, where nudging is disconnected and the model runs only driven by its boundary conditions. We set 4 different spin-up times of 3 h, 12 h, 24 h and 48 h (labelled as NTCOLD, NT12, NT24 and NT48 respectively) to evaluate the impact of the time period over which the nudging is active into the forecast period. Here, the model is initialised from a cold start from GDAS, run through the spin-up period and then followed by the forecast period. Additionally, to evaluate a system that has a more comparable set-up to a typical data assimilation cycle, a fifth spin-up case is set up (NTCYCLE) where the initial conditions are taken from the end of the spin-up period of the previous NTCYCLE run. This simulates a system that runs as a continuously cycling system and relies on data assimilation (a.k.a. nudging) to prevent it from drifting back to its internal climate. All experiments are formulated so that the forecast period starts at 00Z of each day of the monthly period, and the initialisation of the forecast is adjusted for the specific spin-up time (i.e. NT12 will start at the 12Z of the previous day and so on). All forecast periods are of 24 hours, see Table 7 for a summary.

To evaluate the impact of nudging in the spin-up time, NT12, NT24, NT48 and NTCYCLE are run with 3 different nudging configurations that include grid nudging, spectral nudging and free run (no nudging), which are summarized in Table 8. The cut-off wave number in spectral nudging has been set-up to a wavelength of 1000 km, following the conclusions from Chapter 3, where we found that this was the most appropriate value for the latitudes spanned by this European and North African domain (see Figure 20). The experiment

Experiment	Cold Start	Spin-up time	Forecast time
NTCOLD	Yes	3 h	24 h
NT12	Yes	12 h	24 h
NT24	Yes	24 h	24 h
NT48	Yes	48 h	24 h
NTCYCLE	No	24 h	24 h

Table 7: Spin-up times for each experiment. All experiments start from an interpolation from GDAS except for NTCYCLE, which takes its initial conditions from the end of the spin-up period of the previous NTCYCLE experiment.

Experiment	Nudging	WN_X	WN_Y	Length X	Length Y
Fr	Free run	No Spectrum		6600	5200
SpN	Spectral	8	6	1000	1000
GdN	Grid	Full Spectrum		50	50

Table 8: Nudging configuration for each experiment. Wave numbers correspond to a Fourier series where 1 represents the non-oscillatory term of the FFT. This follows the criteria used in the WRF implementation.

with the shortest spin-up NTCOLD is only run with free run to simulate a cold start, allowing a minimal of 3 h before the forecast period. The combination of spin-up times and nudging configurations, plus the Cold Start (NTCOLD) results in 13 experiments per day of each monthly period, which adds up to nearly 1200 model runs.

5.3 RESULTS

The results from these experiments are compared against ERA-interim on different pressure levels for temperature, wind speed and relative humidity. ERA-interim fields matching T+24 h of the forecast period are interpolated horizontally to the WRF grid using the WPS pre-processor. At the same time, WRF fields are interpolated vertically to ERA-interim pressure levels using the UPP post processor, ensuring that the two datasets can be compared in the same grids. To verify the surface fields, we compare maximum and minimum temperature and 24 hour accumulated precipitation against the E-OBS daily dataset. The WRF domain has been selected to match the domain of the E-OBS dataset, so that no horizontal interpolation is needed. We take the maximum and minimum temperature and the accumulation of precipitation at each grid point throughout the forecast period (daily value over the entire month) to compare with the E-OBS dataset. Results are presented only for the month of July 2010 as the three monthly periods evaluated showed comparable results.

5.3.1 Relative humidity

In Figure 21 we depict the BIAS and RMSE (y-axis) for relative humidity at 300, 500, 700 and 850 hPa (panels a, b, c and d, respectively) for each nudging configuration (lines) and spin-up times (x-axis). Nudging, with its two flavours, is able to provide a better forecast than the free run in nearly all cases. This is particularly true for

the Cold Start case, which has a larger RMSE and BIAS than GdN and SpN for NT12, despite being closer to its initialisation in the analysis. This reflects the initial shock that the model suffers when it is initialised from a lower resolution model.

When comparing the experiments for different spin-up times, in almost all cases results are better for the shortest spin-up time, with very similar performance for NT24 and NT48 and a significant worsening for NTCYCLE, which effectively has a much larger spin-up time. Although Fr error grows with the spin-up up time, GdN and SpN are also able to maintain a more stable performance across spin-up times. This highlights the fact that nudging prevents the model from drifting to its internal climate and keeps it closer to GDAS as the simulation

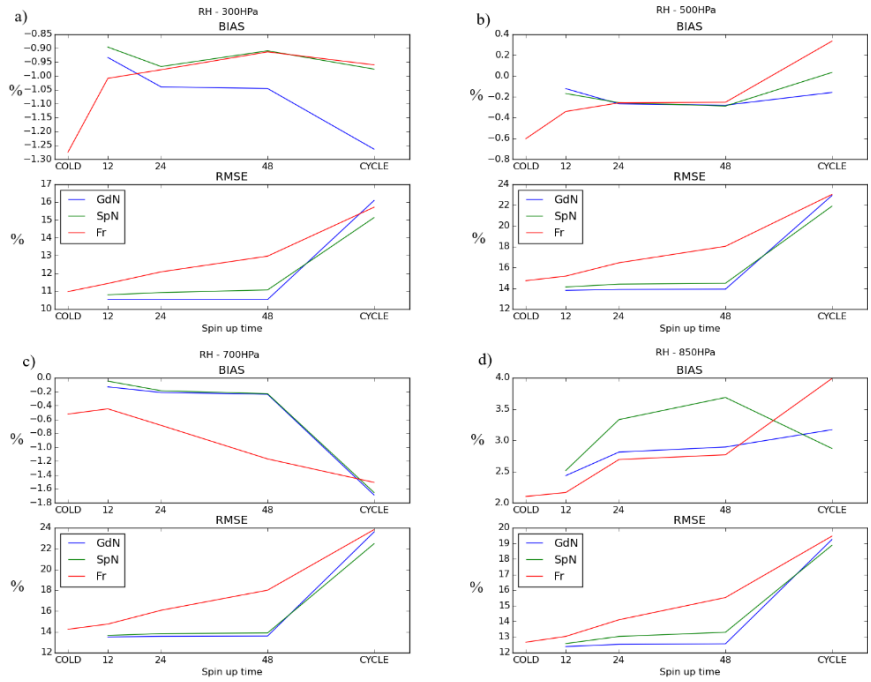

Figure 21: BIAS and RMSE (y-axis) of relative humidity against ERA-interim reanalysis at T+24 after spin-up and for pressure levels 850, 700, 500 and 300 hPa. In the x-axis we present experiments with different spin up times and each coloured line joins experiments using the same nudging technique: GdN (blue), SpN (green) and Fr (red).

progresses. When comparing GdN and SpN, both experiments show very similar results in all levels and in both verification measures, with GdN being marginally better. The only exception is the BIAS at 850 hPa which is larger than for other levels. At higher altitudes, the similar behaviour between GdN and SpN can be explained by the fact that atmospheric fields are smoother. In this case the large scales are the dominant ones and this is the part of the spectrum that is it affected by both nudging techniques. Closer to the surface, all experiments are able to evolve closer to the model internal climate, Fr does not have any forcing and the nudging at GdN and SpN is set to be weaker or non-existent depending on the level, which explains why the BIAS is larger at 850 hPa.

5.3.2 Temperature

Results for temperature, in Figure 22, show a similar behaviour to relative humidity. Here, the Fr experiment has larger BIAS and RMSE compared to GdN and SpN, and BIAS becomes more negative as the spin-up time increases. The only exception is the BIAS at 300, 700 and 850 hPa, which marginally improves from COLD to NT12, but results are small and can be explained by the internal variability of the system. Spin-up times NT12, NT24 and NT48 for GdN and SpN do not show significant differences between them and both provide better performance than Fr. NTCYCLE shows again the worst results, probably due to the error accumulation through the longer spin-up runs. The only exception is the BIAS of the temperature at 300 hPa for Fr, which significantly improves at NTCYCLE. However, compared to other levels, all cases experience a cooling in the BIAS at this spin-up time. This appears to be a secondary effect of a general cooling in the model more than an improvement of the forecast. Similar to cases for relative humidity, there is no clear advantage between GdN and SpN, although these two nudging experiments perform better overall than Fr.

These results provide a similar message to the one found in the relative humidity. While the Fr error grows with the spin-up time, SpN and GdN are able to maintain a more consistent performance across all cases, with NTCYCLE being the only exception. This experiment highlights the fact that the accumulation of error after a long period of

nudging can reduce the performance of the system. GdN and SpN have similar behaviour which, again, can be explained by the fact that at higher altitudes the temperature field has a large scale structure. Also, SpN allows for more high frequency information is less relevant here.

5.3.3 Wind speed

Results for wind shows no significant difference between experiments. For example, for this can be seen at Figure 23 (d) for 700 hPa (note that the vertical scale is very small). Presumably, this is due to the fact that all experiments are able to maintain the synoptic situation reasonably well throughout the simulation. It should be remembered that the model resolution is fairly coarse and the synoptic systems in these latitudes are more predictable and of a larger scale than

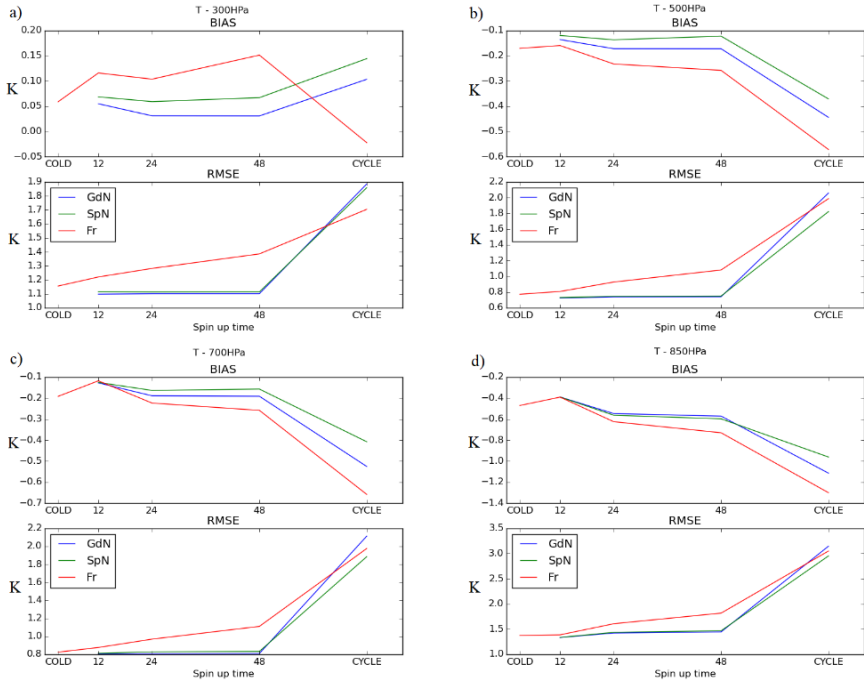

Figure 22: BIAS and RMSE (y-axis) of temperature against ERA-interim reanalysis at T+24 after spin-up and for pressure levels 850, 700, 500 and 300 hPa. In the x-axis we present experiments with different spin up times and each coloured line joins experiments using the same nudging technique: GdN (blue), SpN (green) and Fr (red).

in other latitudes (i.e. tropics). In addition, of the three variables studied in pressure levels, the wind speed is the one that is more dominated by the synoptic scale through geostrophic balance making it less affected by mesoscale variations.

In should be noted that GdN and Fr show a clear reduction of the error for the NTCYCLE case. Although it is tempting to derive conclusions from this plot, the differences are so small that they can be explained by the internal variability or the sampling error.

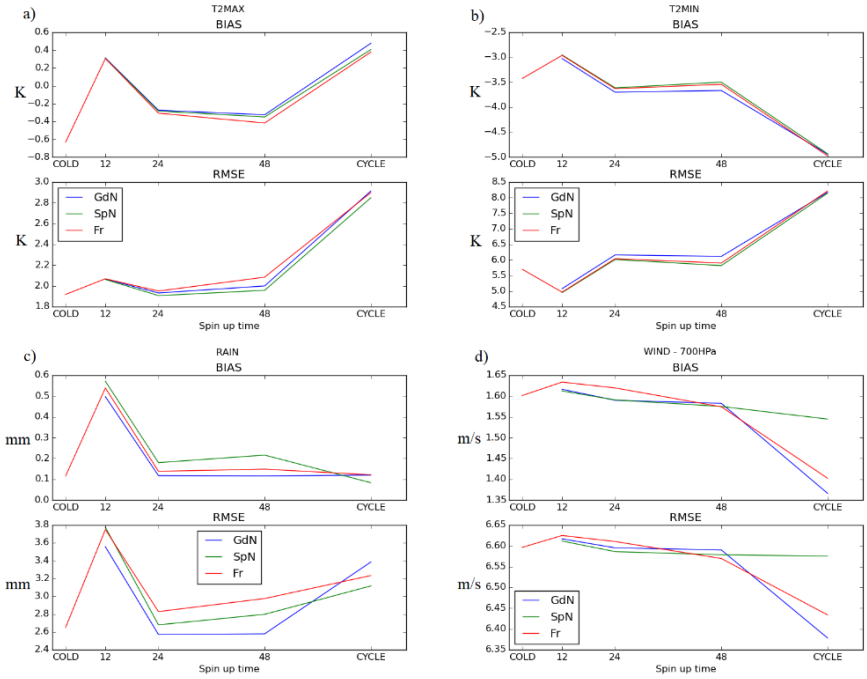

Figure 23: BIAS and RMSE (y-axis) of 2 metre minimum, 2 metre maximum temperature, 24 hour surface precipitation and 700 hPa wind speed. Surface variables are compared against E-OBS and wind speed is compared against ERA-interim at T+24 after spin-up. In the x-axis we present experiments with different spin up times and each coloured line joins experiments using the same nudging technique: GdN (blue), SpN (green) and Fr (red).

5.3.4 Surface variables

Results for maximum and minimum temperature (Figure 23, a, b) present a very similar behaviour between all nudging experiments, with no clear distinction between GdN, SpN and Fr. The COLD and NTCYCLE show poor performance when compared to the other spin-up times. This indicates that some spin-up is needed for the model to minimise the shock from the initial conditions, but not so much that the error builds up after a long spin-up. The shortest spin-up time, NT12, provides the best results of all of them. Conversely, when looking at the precipitation (Figure 23, c), this is the spin-up time that yields the worst results, including COLD, suggesting that longer spin-up times are needed for the precipitation. While surface temperature is more dependent on the synoptic situation (i.e. weather regime), the precipitation strongly relies on water species fields (i.e. water cloud) to be properly initialised. This is reflected here, where the model needs some spin-up time to develop them. Thus, the spin-up time needed to have a better temperature forecast is shorter than that for precipitation. If an optimal nudging set-up is required, in the case of the surface variables, GdN shows marginally better results than the other nudging scenarios.

5.4 SINGLE CASE

From the 3 monthly periods studied, we selected an example case to illustrate the findings from the previous section.

5.4.1 Synoptic setting

A strong convective event occurred on 18th of July 2010 over the coastal areas North and East of the Adriatic Sea. 24 hour accumulation precipitation from TRMM satellite product is depicted in Figure 25 (grey box), which shows three distinct rainfall structures over land and near the coastal areas. We have label them as A, B and C for future reference. The MSLP Figure 24 (a) shows a weak synoptic forcing in the area, with two high pressure areas extending through a large part of Central Europe and the Mediterranean. Although there is some pressure gradient above the Northern part of the Adriatic Sea, this does not result in significantly strong surface winds (Figure 24, b). The high pressure system in Central Europe creates a meridional circulation that brings

cold air from Northern Europe towards the Adriatic Sea. This creates a cut-off low in the North and Eastern Adriatic which can be seen in the

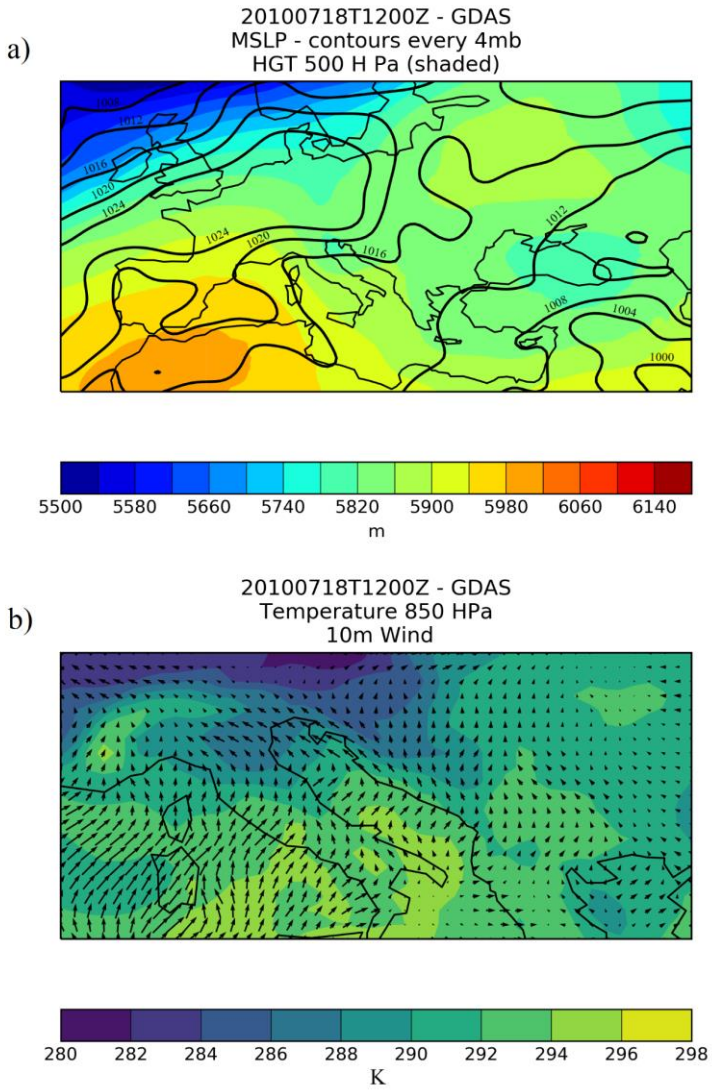

Figure 24: Synoptic setting for the case study on 18th of July 2010, including mean sea level pressure (contour, panel a), 500 hPa geopotential height (shaded, panel a), 10 metre wind (arrows, panel b) and 850 hPa temperature (shaded, panel b)

500 hPa Geopotential height (Figure 24, a) and the 850 hPa temperature (Figure 24, b). At the same time, a thermal low present in northern Africa creates a circulation of warm air across the Mediterranean and toward the Northern Adriatic. The two systems, cold air from the North and warm air from the South, meet creating instability and a strong convective precipitation event in the coastal areas to the north and east of the Adriatic Sea.

5.4.2 Experimental set-up

We use the WRF ARW V3.5 with the same domain and settings described in Section 5.2. Similar to the experiments in 5.2.2, the simulations are set-up to have a spin-up period, where nudging is active, followed by a forecast period, which starts on 18th July 2010 for all experiments. The simulation starting point will depend on the particular settings indicated in Table 7. Particularly, NTCYCLE was started 20 days before the forecast, ensuring that the system is fully spun-up. To test the impact of the different initialisation approaches, for each one the spin-up settings are run in 3 different ways with the nudging settings from Table 8. Similar to Section 5.2, the combination of spin-up times and nudging configurations results in 13 different experiments.

5.4.3 Results

Model results are compared to the TRMM satellite rainfall product and E-OBS observational dataset for 24 h accumulated precipitation between the 18th and the 19th of July 2010. Plots for observations and model output are presented in Figure 25.

The cold start experiment (NTCOLD) is the one with the shortest spin-up time, which clearly helps to reproduce all the precipitation areas present in TRMM. However, when looking at the intensity, NTCOLD produces much more precipitation than the observations, probably due to the shock of the model to the initial condition. NT12 shows a similar result for all nudging configurations, producing an unrealistically large precipitation amount in Northern Italy (area A) and the adjacent alpine region. The convective cells in the Eastern coastal areas (C) of the Adriatic Sea that are present in NT3 are also happening in this set-up. Since all nudging configurations produce a similar result

at NT12, this suggests that 12 hours is not enough time for them to produce a relevant impact in the model simulation. When spin-up time

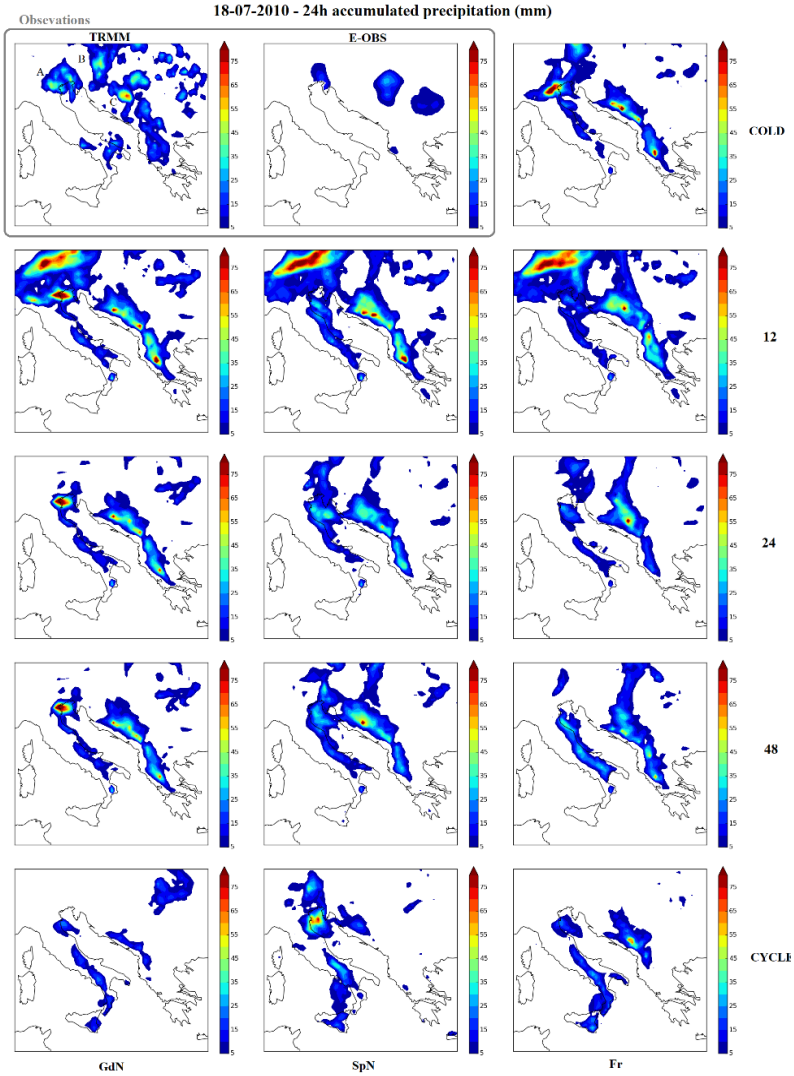

Figure 25: 24 hour accumulated precipitation (mm) for experiments with different combinations of spin up times (rows) and nudging techniques (columns). Observed precipitation from E-OBS and TRMM is also presented in the grey squared box. The areas where the most relevant precipitation occurs have been labelled as A, B, C at the TRMM plot.

is increased to 24 h (NT24) the different nudging configurations start to produce different results between them. For this spin-up time, it is the Fr that produces the most accurate result as compared to GdN and SpN. This indicates that the free run is able to spin-up a bit quicker because there is no nudging that prevents the finer structures from evolving. Spectral nudging is able to reproduce precipitation areas A, B and C reasonably well, but with not enough intensity when compared to the observations, while grid nudging produces too much precipitation everywhere. Doubling the spin-up time to 48 h (NT48) shows that grid nudging produces a very similar result to NT24, with too much precipitation in all areas. For this spin-up time, the free run shows a smoother field, indicating that the information from the initial conditions starts to be lost and the simulation is not able to reproduce the detailed features of the phenomena. On the other hand, spectral nudging is able to reproduce quite accurately the three areas A, B and C the precipitation measured by TRMM and none of the unrealistic ones present in other experimental set-ups. Of all the experiments presented, this is the best performer overall. When the spin-up time is long (NTCYCLE) the accumulation of error from the model simulation becomes very apparent. The three nudging configurations (Fr, SpN and GdN) show a clear degradation of the performance, where not all the precipitation areas seen in the observations are present in the model simulation. SpN is able to produce a precipitation field with more high frequency features than GdN, but they are in the wrong place when compared to the observations. Fr is also able to reproduce some high frequency structures, like the large convective precipitation area in the Eastern Adriatic (area C), but it fails to reproduce the other precipitation features. Finally, GdN produces quite smooth precipitation fields, suggesting the model has drifted to the GDAS climate.

5.5 SUMMARY AND CONCLUSIONS

Spectral nudging has been successfully used as dynamical downscaling technique in many different applications where nearly all involve having the technique activated throughout the whole simulation. To a lesser extent, it has also been used as an initialisation technique in the data assimilation context for limited area models. Examples of this are high profile applications such as the COSMO

regional operational model at the DWD. Complex operational data assimilation systems are usually highly tuned modelling systems which ingest large batches of observations and require significant resources to develop successfully. After the encouraging conclusions from Chapters 3 and 4 we decided to investigate the performance of a modelling system initialised with spectral nudging as a cost effective approach to a fully developed data assimilation scheme.

A limited area model with a domain covering Europe and North Africa is used to run experiments for three different monthly periods changing the spin-up time and using three different approaches: grid nudging, spectral nudging and no nudging. After the spin-up period, in the two first cases nudging is disconnected and the model output produced after the spin-up is evaluated.

When comparing our results to ERA-interim reanalysis on different pressure levels, the grid and spectral nudging are able to maintain a consistent performance for the shortest nudging periods. Meanwhile, the free run experiences a constant degradation, indicating that the nudging approaches are able to prevent model error growth. However, for the longer spin-up times the accumulation of error increases, substantially degrading the performance. When comparing against surface observations, the best performance for the temperature field is achieved in the shortest nudging time (12 h) for all spin-up techniques; meanwhile, the precipitation requires a longer spin-up time of 24 to 48 hours. This is explained by the fact that temperature in the lower troposphere is mostly affected by the particular weather regime, which is imposed by the initialisation and the boundary conditions. The precipitation, however, requires all water species to be initialised (as they are not provided by the initial conditions) which requires a longer time. While the error in temperature is lowest at 12 h, it is still acceptably small between 24 and 48 hours. Thus, considering all the variables together, the range between 24 and 48 hours is the optimal spin-up time. More importantly, it reinforces our conclusions from Chapter 3, where we found that longer spin-up times are needed to improve the forecast skill and, particularly, the same spin up values were found to be the best. It is noteworthy that, although in all cases the

error grows at the longest spin-up time (NTCYCLE), SpN is systematically the best performer in nearly all variables and levels. This shows that though the cycling approach is not the best, shorter spin-up times provide better results. Spectral nudging is the best approach to keep the error from growing in the longer run.

In all the variables studied, the performance of grid nudging and spectral nudging was very similar. There was no clear benefit found in using one over the other. However, in the example case presented of a strong convective event occurring in the Adriatic Sea, it can be seen that the experiment with spectral nudging and 48 h of spin-up is the best at representing the precipitation patterns seen in the observations. It should be noted that to find the example case we evaluated 180 days from different seasons and the presented case was the only one where a clear distinction between the spectral nudging and grid nudging behaviour could be observed. Also, we could not find a case where grid nudging performed better than spectral nudging. This suggests that both techniques give the same benefits in most cases, but that spectral nudging might be able to perform better in some weather situations, more evidence should be presented to support this conclusion.

Finally, it should be noted that the observational dataset used for verification at the surface, E-OBS, clearly shows a large scale, smooth, pattern that does not reflect detailed spatial variations. An example of this can be seen in Figure 25 (grey box) where we present the precipitation for our example case. The measured 24 h accumulated rainfall from E-OBS has a precipitation structure that is quite smooth and has a much lower intensity when compared to TRMM (Figure 25, grey box). Other variables from E-OBS present the same spatial structure (not shown). Results for our test case indicate that spectral nudging is likely to produce more high frequency information than grid nudging; however, the nature of this observational dataset makes it difficult to evaluate this feature properly. A higher resolution observational dataset called MESCAN (issued by MeteoFrance) has been released at the time of writing this work, which opens the possibility to compare similar experiments with finer scale measurements in the future.

6 PhD summary and conclusions

Nudging, and particularly spectral nudging, is a popular technique used in different applications that range over multiple spatial and temporal scales. Its most attractive feature is that it is able to keep a LAM close to a reference field while preventing it from drifting to its own climate. This is particularly useful when the modelling domain is large. Spectral nudging, one of the variations of this technique and the focus of this work, adds further flexibility by bringing the possibility to select the scales on which the model is nudged.

In Chapter 1 we present a literature review of the existing work in this area, which shows that despite the many studies which use spectral nudging, no systematic study of the technique itself has been done before. When selecting the values of the tuning parameters, nearly all authors base their decisions on the features like the domain design or the forcing data (i.e. domain resolution or size). In our work we seek to deepen the understanding of the technique and how it can alters the model simulation. For that, we focus on studying the impact of two of these parameters: first, the cut-off wave number, that stablishes the scales where nudging is applied, and second, the spin-up time, or how much time the model requires to establish a balance with the nudging effect.

We perform our study in two different regions, one in the mid-latitudes and another in a tropical setting (presented in Chapters 3 and 4 respectively). We include a variety of synoptic situations which are representative of the typical weather regimes for each of the modelled regions. Results show that spectral nudging needs a longer time to spin up than grid nudging, primarily because the model is allowed to stay closer to its own climate. It was observed that the optimal the spin-up time is longer as the modelling domain gets closer to the equator, being 24 h to 48 h in mid latitudes to 72 h to 96 h in the tropics. We speculate that in tropical settings spectral nudging needs more time to spin up because some variables, like the cloud water fraction, that are not

provided by the initial conditions and they need to be evolved by the model dynamics. Tropical regions are typically more covered with clouds than mid-latitudes and, therefore, more time is needed to spin up all the water species associated with them.

A spectral analysis of the results indicates that spectral nudging is very efficient at separating the nudged scales from the ones that are not nudged. For most cut-off wave numbers the experiments show the same power spectrum as grid nudging below the cut off wave number and the same as the free run case above it. This indicates that spectral nudging allows the model to develop the same high frequency information as the free run with the synoptic scales being adequately constrained. The only exception is for very large cut off wave numbers where spectral nudging starts to approximate the grid nudging behaviour and the higher scale features are severely damped.

Comparison against observations shows that the biggest reduction in error happens for the first cut-off wave numbers, and that not much benefit is obtained nudging higher scales after a certain point. We argue that the optimal cut off wave number should be selected so that a substantial part of the error is reduced, but not so much that the finer spatial details contributed by the LAM are severely affected. We estimate the optimal cut off wave numbers (in Chapters 3 and 4 we propose two different methodologies) to be the Rossby Radius of Deformation for the area, being 1000 km in mid-latitudes, and increasing up to 1500 km near the equator. Also, our findings suggest that, as the synoptic forcing gets weaker in the tropics, convection starts to be more relevant than the synoptic forcing for some variables, which suggests that it can be beneficial to have different cut-off wave numbers for each nudged variable. We propose a new spectral nudging approach where a different cut-off wave number is used for each variable and our tests on 4 different hurricane cases show that this is the best performing set up.

In summary, our results indicate that the parameter selection (spin up time and cut-off wave number) can be justified by the physical behaviour of the system and not by parameters of the modelling design

such as model size, resolution or properties of the driving dataset. In each chapter we presented case studies that support our findings.

Finally, in Chapter 5, we study the application of spectral nudging as an initialisation technique, to mimic the functionality of more complex data assimilation implementations. Although spectral nudging is a much simpler and less expensive technique, we use conclusions from previous chapters to implement a system that would ingest data from analysis fields in an *assimilation window*, determined by the spin-up time where nudging is active, and we evaluate its performance in the *forecast step*, when nudging is not active. Comparisons against different observational datasets show that, for a mid-latitude domain, spin up times around 24 h to 48 h are the best performing ones, supporting our conclusions from Chapter 3. However, no clear advantage was found between spectral nudging and grid nudging, showing a remarkably similar performance. We speculate that the surface observational dataset might not have the sufficient spatial detail to reveal the differences between the two. However, it should be mentioned that numerous cases for different time periods were studied and the visual analysis of the forecasted precipitation supports the idea that, when nudging is disconnected, the model quickly drifts to its own climate, losing the benefits gained at the spin-up window.

7 Appendixes

7.1 RESÚMENES

7.1.1 Resumen extenso en castellano (summary in Spanish)

7.1.1.1 Estado de la cuestión

Nudging, en sus múltiples variantes, ha sido utilizado en diferentes aplicaciones de la predicción numérica meteorológica. En esencia, esta técnica relaja la solución de una ecuación diferencial hacia un valor de referencia, más preciso que el modelo en sí, en cualquier punto dado de la malla. Como resultado, los puntos en las cercanías alteran su predicción para adaptarse al valor de referencia y, por tanto, producen una predicción más realista que sigue en consistencia con las ecuaciones físicas del modelo. Una de las primeras aplicaciones de esta técnica fue en el campo de la asimilación de datos (Anthes, 1974) y, a pesar de que en estos días de utilizan técnicas mucho más complejas, el *nudging* ha sido utilizado en la predicción operativa global del tiempo, en centros como el Met Office (Lyne et al., 1982), y regional, también en el Met Office (Bell, 1986) y el Deutsche Wetterdienst (Schraff, 1996, 1997).

Cuando se dispone de un análisis definido en toda la malla del modelo, el *nudging* se suele aplicar en todo el dominio del modelo, imponiendo una ligadura en su solución en todos sus puntos (Davies and Turner, 1977; Stauffer and Seaman, 1990). Recientemente, una variación del *nudging* llamada *spectral nudging* (Miguez-Macho et al., 2004; von Storch et al., 2000; Waldron et al., 1996) ha ido creciendo en popularidad. En esta variante, solo una parte del espectro espacial de la variable predictiva del modelo es forzada hacia el espectro equivalente del campo de referencia, permitiendo que la otra parte del espectro evolucione con mayor libertad. En la mayoría de aplicaciones, el *spectral nudging* se aplica en las escalas sinópticas, permitiendo que el modelo evolucione libremente en las escalas de mayor frecuencia espacial.

Una de las aplicaciones típicas del *spectral nudging* es la predicción climática regional dinámica (RCM, por sus siglas en inglés)

(Miguez-Macho et al., 2004, 2005; von Storch et al., 2000), donde se suele utilizar como condición de contorno una estimación de la circulación atmosférica global (i.e. un reanálisis global). Es un hecho conocido que, cuando este tipo de sistemas tienen una malla grande, su solución puede divergir substancialmente de su condición de contorno (Davies, 1976, 1983), y que las ondas atmosféricas más largas, que no son correctamente representadas en las fronteras del modelo, rebotan y alteran la circulación general en otras partes del dominio (Miguez-Macho et al., 2004). Varios estudios han mostrado que el *spectral nudging* es capaz de mantener la estructura sinóptica del RCM en concordancia con su condición de contorno mientras que, al mismo tiempo, desarrolla sus propias estructuras locales (Miguez-Macho et al., 2004, 2005). Algunos autores (Braun et al., 2012; Colin et al., 2010; de Elía et al., 2008; de Elía and Côté, 2010; Lucas-Picher et al., 2013; Sanchez-Gomez et al., 2009) han estudiado el impacto del *spectral nudging* en RCMs mostrando que esta técnica es capaz de reducir la variabilidad interna del modelo. Otros trabajos han demostrado así mismo que la aplicación del *spectral nudging* en RCMs no altera significativamente las escalas espectrales donde la técnica no es aplicada (Berg et al., 2013; Radu et al., 2008). Más recientemente, se ha mostrado que el *spectral nudging* mejora la estimación de la frecuencia de ciclones tropicales durante la temporada de huracanes gracias a una mejor representación de los patrones de larga escala, y en particular a la circulación monzónica en la baja troposfera (Choi and Lee, 2016).

El *spectral nudging* también ha sido utilizado en otros tipos de aplicaciones: reducción del error de los vientos en superficie forzando el modelo a un campo de referencia por encima de la capa límite(Vincent and Hahmann, 2015), mejorar la simulación de un tifón tropical(Wang et al., 2013), recuperar características de la pequeña escala en un modelo geostrófico de dos capas cuando se fuerza a un campo de larga escala (Katavouta and Thompson, 2013), mejorar la simulación de un campo de vórtices tras relajar el modelo a una climatología observacional (Stacey et al., 2006), mejorar la modelización de la cobertura nubosa (Meinke et al., 2006) y preservar la solución del modelo al mismo tiempo que se desarrolla la turbulencia

local (Yamaguchi et al., 2013). El *spectral nudging* también ha sido utilizado para la asimilación de datos (Stauffer et al., 1991; Stauffer and Seaman, 1994).

7.1.1.2 Motivación

En todos los trabajos presentados en el apartado anterior, los valores de corte del número de onda (a partir de donde se dejar de aplicar el *spectral nudging*) se eligen basándose en las preferencias de los investigadores. Algunos autores seleccionan el número de onda más bajo posible y, por tanto, solo fuerzan las escalas más largas (Miguez-Macho et al., 2004), asegurando una interferencia mínima en la dinámica del modelo. Otros autores usan un valor relacionado con el objetivo de la simulación o el campo el campo de referencia. Por ejemplo, en un trabajo se fuerzan las escalas mayores de 1500 km basándose en las escalas que quieren evaluar (Separovic et al., 2012); en otro, se fuerzan las escalas mayores a 2000 km debido a que esta es la resolución efectiva del modelo utilizado como condición de contorno (Liu et al., 2012); y en otro caso se fuerzan las escalas mayores a 300 km debido a que esta es la resolución típica de un modelo climático global (Omrani et al., 2013). En los pocos trabajos en los que evalúan diferentes valores de corte, algunos autores destacan que el número de onda más apropiado está aproximadamente en 1000 km (Liu et al., 2012; Wang and Kotamarthi, 2013). Cabe notar que en Liu et al. (2012) se realizaron algunas pruebas de sensibilidad para evaluar las diferencias entre el *grid nudging* y el *spectral nudging*, pero el conjunto de variables utilizados era diferente entre las dos técnicas. En resumen, lo expuesto muestra que no existe un criterio unificado en la comunidad científica sobre cómo elegir el valor más apropiado para el número de onda de corte cuando se utiliza *spectral nudging*.

En el presente trabajo investigamos dos parámetros del *spectral nudging* que no han sido estudiados en detalle. En primer lugar, el número de onda corte y el impacto que tiene en la predicción de un modelo meteorológico al seleccionar diferentes valores, con particular énfasis en el efecto que tiene sobre la estructura espectral de la solución del modelo. Este parámetro determina que parte del espectro espacial de los campos predichos por el modelo es forzado hacia los campos de

referencia y cual evoluciona sin restricciones. Nuestros resultados muestran que este parámetro tiene un impacto decisivo en el resultado de la predicción y, a pesar de ello, no existe un criterio unificado sobre cómo elegir el valor más apropiado. En segundo lugar, a lo largo de nuestros experimentos también estudiamos el tiempo que el modelo necesita para equilibrar el impacto del *Nudging* (comúnmente conocido como tiempo de *spin-up*). Este es el tiempo que se debe ejecutar una simulación previa antes de comenzar a evaluar los resultados. Si el tiempo es demasiado corto el modelo todavía está equilibrando el impacto producido por la técnica y si es demasiado largo la acumulación del error numérico podría ser demasiado grande. El número de onda de corte es particularmente importante cuando se utiliza *spectral nudging* para la predicción climática regional mientras que el tiempo de *spin-up* es muy relevante cuando se estudian casos individuales o cuando el *spectral nudging* se utiliza como un sustituto de la asimilación de datos.

La estructura de la tesis es como sigue, en el capítulo 2 describimos la diferentes técnicas de *Nudging* utilizadas (este capítulo, eminentemente técnico, se ha obviado en este resumen en castellano). En el capítulo 3 estudiamos el impacto del *spectral nudging* en un modelo con una malla situada en latitudes medias mientras que en el capítulo 4 realizamos un análisis similar con una malla situada en latitudes tropicales. En el capítulo 5 estudiamos la idoneidad del *spectral nudging* como técnica de inicialización emulando las características de la asimilación de datos. Por último, en el capítulo 6 se hace un resumen de todos los trabajos realizados.

7.1.1.3 Spectral nudging en latitudes medias

Nuestro sistema de modelización consiste en un modelo de área limitada localizado en el Sur Oeste de Europa, con una gran parte del dominio sobre el Océano Atlántico para incluir los sistemas sinópticos que afectan a esta región. Modelamos 3 periodos mensuales que representan condiciones típicas de verano, invierno y otoño utilizando diferentes números de onda de corte del *spectral nudging* inicializando cada experimento en cada día del mes y ejecutándolo durante 96 horas. Al mismo tiempo, también incluimos dos experimentos con *grid*

nudging y *free run* (sin *nudging*) como referencia. Enfocamos nuestro estudio en comparar el resultado de nuestro modelo con el modelo de condiciones de contorno, el cual es también usado como campo de referencia en el *nudging*.

En los experimentos con *spectral nudging* el RMSD (raíz cuadrada de la distancia cuadrática media, por sus siglas en inglés) con respecto al horizonte de simulación se estabiliza tras 36/48 horas desde la inicialización, mostrando un comportamiento ruidoso en las primeras horas de predicción, siendo este mayor que en las simulaciones con *grid nudging* y menor que en los casos con *free run*. A pesar de que la fuerza del *nudging* usada es la misma en todos los experimentos, la ligadura impuesta en el modelo es mayor en el caso del *grid nudging* debido a que todo el espectro esta forzado, y las amplitudes de cada uno de los modos se ven atenuadas incluso cuando el campo de referencia no dispone de información en las escalas más finas. Debido a esto, el modelo alcanza un equilibrio entre el efecto del *nudging* y su propio clima mucho antes que con el *spectral nudging*, donde una parte del espectro no se ve afectada. El experimento con *free run*, que no está forzado, necesita el mayor tiempo de *spin-up*, superando las 96 h de duración de las simulaciones.

La estructura espectral de las variables analizadas muestra que el *spectral nudging* es capaz de alterar los modos de onda más largos por debajo del número de onda de corte haciéndolos iguales a los equivalentes en la condición de contorno. Al mismo tiempo, los modos por encima del número de onda de corte mantienen la misma magnitud que en las simulaciones sin *nudging*. Esto sugiere que, al usar *spectral nudging*, la divergencia entre el LAM y su condición de contorno se debe al desarrollo de modos de alta frecuencia espacial que no están presentes en los campos de referencia. Por este motivo, el RMSD del modelo con respecto a dichos campos es mayor para los experimentos con menor número de onda de corte, y cuanto mayor se hace este parámetro mayor similitud existe entre los dos. Por tanto, el experimento con free run es el que posee el mayor RSMD y, a su vez, el experimento con *grid nudging* tiene el menor, estando los casos con *spectral nudging* en medio de los dos. Nuestros experimentos utilizan

una fuerza de *nudging* de 1 h-1 y cuando los experimentos se realizan con intensidades de *nudging* menores tales como 3 h-1 y 6 h-1, el experimento con *grid nudging* es capaz de generar mayor información de pequeña escala. Sin embargo, su amplitud siempre es menor que las estructuras equivalentes en los experimentos con *spectral nudging*, donde tienen la misma magnitud que *free run*. Esto reafirma la idea de que el *spectral nudging* es mucho más eficiente que el *grid nudging* a la hora de permitir al LAM que genere información de pequeña escala, y de la misma magnitud que los experimentos donde no es aplicado.

El comportamiento del RMSD con respecto al número de onda de corte muestra claramente que el error desciende rápidamente a medida que el número de onda aumenta, y que gran parte de dicha reducción ocurre aplicando *nudging* en las escalas más largas. Para valores por encima de un determinado punto, el RMSD apenas cambia y sus pequeñas variaciones se explican por el hecho de que la información de pequeña escala del LAM está siendo atenuada. Hemos estimado el punto de inflexión en la tendencia del RMSD alrededor de 1000 km, y este valor es consistente en todos los niveles del modelo hasta 10 km de altitud.

Una explicación física de este resultado es que la escala de 1000 km coincide con el Radio de Deformación de Rossby, que es comúnmente interpretado como el punto donde los efectos rotacionales en la atmósfera comienzan a ser menos relevantes que la convección vertical, marcando la transición de la escala sinóptica a la escala convectiva. Al elegir un valor de 1000 km como número de onda de corte en *spectral nudging*, estamos forzando de forma efectiva la escala sinóptica al mismo tiempo que se permite que la pequeña escala se desarrolle libremente. En el trabajo mostramos un caso de ejemplo que muestra que los experimentos con números de onda de corte cercanos a 1000 km producen los resultados que más se acercan a las observaciones.

7.1.1.4 Spectral nudging en latitudes tropicales

En este trabajo se busca verificar si las conclusiones expuestas en el capítulo anterior también son válidas en las latitudes tropicales. Para

ello, utilizamos el modelo WRF con una malla centrada en el Golfo de México que incluye una gran parte del Atlántico Norte, donde se originan las tormentas tropicales que posteriormente evolucionan en huracanes. El modelo se ejecuta durante 96 horas iniciado durante cada uno de los días del periodo que va de finales de agosto a finales de septiembre de los años 2010 a 2015; esta parte del año es la que contiene mayor actividad de huracanes. La temporada de 2010-2012 es una de las más activas de la historia reciente mientras que el periodo 2012-2015 estuvo por debajo de la media, lo que permite incluir diferentes tipos de casos y situaciones en nuestro estudio. Para cada día simulado se utilizaron 10 configuraciones distintas: 8 con *spectral nudging*, con diferentes números de onda de corte, una con *grid nudging* y otra con *free run*.

La evolución temporal del RMSD indica que el tiempo de spin-up donde el modelo equilibra su clima interno con el efecto del *nudging* está alrededor de 72 h a 96 h, siendo el doble de la obtenida para latitudes medias. Esto podría estar relacionado con la naturaleza, más convectiva, de los fenómenos típicos de estas latitudes. En particular, se debe recordar que las condiciones iniciales del modelo no contienen ninguna de las especies del agua, aparte del vapor de agua. La troposfera es generalmente más alta en las latitudes tropicales lo cual puede implicar un mayor tiempo para inicializar dichas variables que en las latitudes medias.

Nuestro análisis de la estructura espectral de la solución del modelo indica que el *spectral nudging* es capaz de separar las escalas forzadas de las que evolucionan libremente, haciendo que el modelo tenga la misma estructura de que los experimentos con *grid nudging* por debajo de numero de onda de corte y que el *free run* por encima. Al mismo tiempo, *nudging* mejora notoriamente la predictibilidad del sistema y su aplicación en las escalas más largas produce la mayor reducción del RSME. Cuando se extiende el *spectral nudging* a escalas más pequeñas el RMSE apenas cambia, y ello ocurre a expensas de eliminar la información de alta frecuencia que aporta el LAM. Esto es particularmente apreciable en los casos particulares de huracanes presentados, donde las simulaciones con los números de onda de corte

mayores no son capaces de reproducir la presión en el centro, siendo esta no lo suficientemente baja, y los vientos, siendo estos no lo suficientemente altos.

Nuestros resultados sugieren que el número de onda de corte se debe elegir de modo que aporte una reducción significativa del RMSE, pero sin que ello atenúe las ondas de alta frecuencia aportadas por el LAM. Nuestro estudio indica que el valor óptimo ocurre a diferentes escalas para cada variable, siendo este 2000 km para la temperatura, 1100 km para el viento y 700 km para la humedad. Estos valores encajan con las características sinópticas de cada una de ellas, ya que la temperatura tiene una estructura espacial de larga escala, la humedad está muy afectada por la convección y el viento posee un comportamiento intermedio. Si se realiza el promedio entre los tres valores, el valor resultante es 1300 km, que es ligeramente mayor que el Radio de Deformación de Rossby en latitudes medias (1000 km) y concuerda con el hecho de que la fuerza de Coriolis es más débil cerca del Ecuador. Esto refuerza nuestras conclusiones del capítulo anterior, en las que indicamos que el número de onda de corte óptimo está relacionado con las características sinópticas del área modelada y no con los parámetros específicos del diseño del experimento, como la resolución o el tamaño de la malla.

Por último, en este capítulo proponemos una nueva variación sobre el *spectral nudging*, donde utilizamos diferentes números de onda de corte para cada variable. Esta configuración funciona sistemáticamente mejor en todas las variables y casos evaluados. Esto sugiere que este nuevo enfoque podría permitir diseñar experimentos con menor dependencia de su localización en latitud, o de los fenómenos que se quieren modelar.

7.1.1.5 Spectral nudging como técnica de inicialización de modelos de área limitada

El *spectral nudging* es comúnmente utilizado como técnica de anidamiento, en la que permanece activo durante toda la simulación. En una menor medida, también es utilizado como técnica de inicialización, emulando el comportamiento de las técnicas de

asimilación de datos en modelos de área limitada, siendo un ejemplo de esto el sistema operacional de modelo regional COSMO en el Deutscher Wetterdienst (Centro nacional de meteorología alemán). Este tipo de usos aplicaciones requieren un gran esfuerzo en desarrollo y ajuste, donde se utiliza un gran número de observaciones distintas. Basándonos en los resultados de los capítulos anteriores, aquí evaluamos si es posible utilizar el *spectral nudging* en un ajuste más simplista pero igualmente efectivo que permita ahorrar tiempo de desarrollo sobre un sistema de asimilación de datos más complejo.

Diseñamos un sistema experimental que cubre Europa y el Norte de África y ejecutamos diferentes experimentos a lo largo de tres periodos mensuales distintos. Por cada día del periodo mensual utilizamos 3 técnicas de *nudging* distintas: *grid nudging*, *spectral nudging* y *free run* (no *nudging*) y 4 tiempos de *spin-up* diferentes que van desde 3 horas hasta varios días. Después del periodo de *spin-up* el *nudging* es desconectado y realizamos la verificación sobre las primeras 24 horas sin forzamiento.

Al comparar los resultados contra los reanálisis del ERA-interim en diferentes niveles de presión, el *grid nudging* y *spectral nudging* son capaces de mantener un error constante para todos los tiempos de *spin-up* más bajos, mientras que el *free run* sufre una degradación constante a medida que la inicialización crece en el tiempo. Esto indica que ambas técnicas de *nudging* son capaces de impedir que el error crezca a medida que el modelo avanza en la simulación, al menos en los tiempos más cortos. En los tiempos más largos, el error comienza a aumentar, degradando sustancialmente la simulación. Al comparar los resultados contra observaciones en superficie, los mejores resultados en temperatura ocurren para los tiempos más cortos (12 h) en todas las técnicas de *nudging* utilizadas, mientras que la precipitación requiere tiempos algo más largos, de entre 24 h y 48 h. Esto se explica por el hecho de que la temperatura en la baja troposfera está regida principalmente por la situación sinóptica, que está impuesta en el modelo por las condiciones de contorno. La precipitación, sin embargo, requiere que todas las especies del agua estén correctamente inicializadas (las condiciones iniciales solo proporcionan el vapor de

agua) y esto requiere un tiempo mayor. Dado que el error en la temperatura es aceptable para los *spin-ups* entre 24 y 48 horas, esto hace que estos valores sean los óptimos para inicializar el modelo. Es importante recalcar que este resultado refuerza nuestras conclusiones del capítulo 3, donde se indica que hacen falta tiempos de *spin-up* más largos para las simulaciones con *spectral nudging*, y donde encontramos los mismos valores óptimos.

Al contrario que en capítulos anteriores, en todos los casos estudiados, el *grid nudging* y el *spectral nudging* muestran resultados muy similares, sin una clara ventaja entre las dos técnicas, y siendo ambos superiores al *free run*. Se debe recalcar que las estadísticas en superficie han sido calculadas utilizando la base de datos observacional E-OBS que es de notoria baja resolución. El estudio de los resultados de los experimentos sugiere que el *spectral nudging* es capaz de generar campos con mayores detalles de pequeña escala que el *grid nudging*. Sin embargo, la baja resolución de la E-OBS no permite evaluar si esto supone una ventaja real entre las dos técnicas. En el momento de escribir este trabajo, se acaba de publicar una nueva base de datos observacional de mayor resolución, MESCAN (Meteo France), que abre la posibilidad a evaluar experimentos similares con observaciones con mayor detalle espacial.

7.1.2 Short summaries

7.1.2.1 Short summary in English

The present works studies the spectral nudging technique aiming to improve the accuracy of the forecasts of atmospheric limited area models. It allows to impose a forcing over a subset of the spatial spectral scale, typically the largest one, while it allows the limited area model to develop its own dynamics in the unconstrained ones. Despite a substantial number of works has been published on the topic, not many have studied the technique in a systematic way.

A great part its extension studies two relevant parameters from spectral nudging. Firstly, the cut-off wave number, which effectively separates the nudged scales from the free running ones. And, secondly,

the spin-up time, which determined how much time is needed to reach a balance between the nudging force and the model internal climate.

Our results show that the optimal cut-off wave number coincides with the Rossby Radius of Deformation, both in mid and tropical latitudes, suggesting that this parameter is related with the dynamic characteristics of the modelled area, and not with features of the experiment design. The optimal spin-up time is found to be 24/48 h for mid latitudes and 72/96 h for tropical latitudes.

At the same time, we have studied the suitability of spectral nudging as a poor man's data assimilation technique, which are commonly used to improve the initialization of the numerical weather prediction models. Our results indicate that it is beneficial to use some nudging technique at the beginning of the simulation, but we have not found relevant differences between grid nudging and spectral nudging.

7.1.2.2 Resumen corto en español (Short Summary in Spanish)

Esta tesis evalúa la técnica de *spectral nudging* como herramienta para mejorar la predicción de los modelos meteorológicos de área limitada. Ésta permite forzar el modelo meteorológico solo en las longitudes de escala donde el modelo de condiciones de contorno es preciso (larga escala) y deja que desarrolle su propia dinámica en el resto del espectro (corta escala). Pese a que se han publicado un gran número de trabajos de investigación utilizando esta técnica, muy pocos se han centrado en caracterizar su impacto de forma sistemática.

Este estudio dedica la mayor parte de su extensión a estudiar el impacto de dos parámetros del *spectral nudging*. En primer lugar, el efecto del número de onda donde se establece la separación entre las escalas anidadas y las escalas libres. Y en segundo, el tiempo necesario desde la inicialización del modelo hasta que el clima del modelo se encuentra en equilibrio con el efecto del anidamiento espectral

Nuestros resultados muestran que el número de onda de corte óptimo coincide con el Radio de Deformación de Rossby, tanto en latitudes medias como tropicales, sugiriendo que este parámetro está

ligado a la dinámica atmosférica del área simulada, y no con cuestiones relativas al diseño del experimento. Así mismo el tiempo óptimo de inicialización resulta estar sobre 24/48 h en latitudes medias y 72/96 h en latitudes tropicales.

Complementariamente, también se ha estudiado la idoneidad del anidamiento espectral como técnica de asimilación de datos. Esta sirve para mejorar la inicialización de los modelos meteorológicos cuando realizan predicciones a corto plazo. Nuestros resultados indican que es beneficioso incorporar algún tipo de *nudging* al comienzo de la simulación, pero no se aprecian diferencias notables entre el *grid nudging* y el *spectral nudging*.

7.1.2.3 Resumo corto en galego (Short summary in Galician)

A presente tese estuda a técnica de *spectral nudging* como ferramenta para mellorar a predición de modelos meteorolóxicos de área limitada. Esta permite forzar o modelo so nas lonxitudes de escala onde o modelo de condición contorno é mais preciso (larga escala) e deixa que este desenrole a sua propia dinámica no resto do espectro (curta escala). A pesares de existir un gran número de publicacións sobre esta cuestión, moi poucos estudan esta técnica dunha maneira sistemática.

Este traballo dedica a meirande parte da súa estensión a estudar o impacto de dous parámetros de gran relevancia no *spectral nudging*. En primeiro lugar, o efecto do número de onda de corte, onde se establece a separación entre a escalas aniñadas es as escalas libres. E en segundo lugar, o tempo necesario dende a inicialización ata que o efecto do aniñameto establece un equilibrio co clima interno do modelo.

Os nosos resultados mostran que o número de onda de corte óptimo coincide co Radio de Deformación de Rossby, tanto en latitudes medias coma tropicales, suxerindo que dito parámetro está máis ligado a dinámica atmosférica da área simulada que con cuestións relativas ao deseño do experimento. Do mesmo xeito, o tempo óptimo de inicialización do modelo resulta estar entre 24/48 h en latitudes medias e 72/96 h en latitudes tropicales.

Finalmente, tamén se estudou a ideonidade do aniñamento espectral como técnica de asimilación de datos. Dita serve para mellorar a inicialización dos modelos meterolóxicos cando se realizan prediciones a curto prazo. Os nosos resultados indican que é beneficioso incorporar algún tipo de aniñamento ao comenzo da simulación, pero non se atoparon diferencias notables entre o *grid nudging* e o *spectral nudging*.

7.2 DESCRIPTION OF HURRICANE CASES

The following texts have been extracted from the reports of the National Hurricane Center, which include a synoptic description for each hurricane studied in Section 4.4. They are reproduced here in a form that is very similar to the original documents, although the texts have been slightly changed from the original to ensure readability by removing references to figures and tables.

References to the reports are indicated at the beginning of each section. Note that the originals have been written in American English, where some words have different spellings.

7.2.1 Hurricane Earl

Text extracted from Cangialosi (2011)

"Earl originated from a strong tropical wave that departed the west coast of Africa on 23 August. A closed-surface circulation developed along the wave axis by 0000 UTC 24 August and the associated thunderstorm activity became organized as the low moved south of the Cape Verde Islands later that day. By early 25 August, the low acquired sufficient convective organization to be considered a tropical depression by 0600 UTC, when centered about 200 n mi west-southwest of the Cape Verde Islands. The convective curved banding expanded and became better organized later that day, and the system strengthened to a tropical storm by 1200 UTC.

Strong subtropical ridging over the eastern Atlantic steered Earl westward to westnorthwestward at a forward speed, between 15-20 kt, for the next few days. Meanwhile, the tropical storm strengthened

gradually over sea surface temperature of 28°-29° C and in an environment of light to moderate shear. Data from an Air Force Reserve reconnaissance aircraft indicate that Earl became a hurricane by 1200 UTC 29 August, when centered about 220 n mi east of the northern Leeward Islands. Around that time, the cyclone neared a weakness in the subtropical ridge caused by Hurricane Danielle to its west, and Earl slowed and gradually turned northwestward. During this process, the hurricane experienced rapid intensification. A bandedtype eye became apparent in radar imagery from Guadeloupe and St. Maarten around 0000 UTC 30 August, and Earl strengthened to a Category 3 hurricane about 12 h later when it was located very near the northern Leeward Islands.

Data from both NOAA and Air Force hurricane hunter aircraft, along with satellite imagery, indicate that Earl intensified by 40-kt over 24 h, becoming a Category 4 hurricane by 1800 UTC 30 August. Shortly after reaching that status, Earl began a concentric eyewall replacement cycle that was well observed in both the San Juan Doppler radar and aircraft flightlevel wind data. This cycle halted the intensification process and Earl remained a 115-kt hurricane for the next 24 h. Southwesterly shear increased late on 31 August, which resulted in Earl weakening back to a Category 3 hurricane by 0000 UTC 1 September. Earl weakened a little more during the morning hours of 1 September while passing directly over NOAA buoy 41046, which reported a minimum pressure of 943 mb around 0700 UTC, and a sustained wind of 71 kt with a gust to 87 kt immediately prior to the minimum pressure report. However, by that afternoon the eye became more distinct and deep convection increased and gained symmetry, presumably due to a decrease in shear. Earl re-intensified to category 4 strength by 1800 UTC 1 September and reached its peak intensity of 125 kt 12 h later, when it was located about 380 n mi southeast of Wilmington, North Carolina.

Earl then rapidly weakened as it turned northward and fell below major hurricane status by 0000 UTC 3 September. The rapid weakening was likely due to the combination of another concentric eyewall replacement cycle, an increase in south-southwesterly shear, cooler

waters, and a drier environmental air mass. Earl weakened to a Category 1 hurricane later on 3 September while passing offshore of the mid-Atlantic and northeast United States coastline. The cyclone passed about 75 miles east of Cape Hatteras, North Carolina and 70 miles west of NOAA buoy 41001, which reported a sustained wind of 52 kt and a gust to 64 kt around 0900 UTC 3 September. Air Force reconnaissance data indicate that Earl weakened to a tropical storm by 0000 UTC 4 September, while centered about 130 n mi south-southeast of the eastern tip of Long Island, New York.

Earl made landfall as a 65-kt hurricane about 3 h later near Liverpool, Nova Scotia in Canada and as a 60-kt tropical storm on Prince Edward Island around 1900 UTC 4 September. Earl became extratropical by 0000 UTC 5 September in the Gulf of St. Lawrence, as it interacted with an upper-level low; this interaction also caused the system to slow down and turn toward the north. Meanwhile, the cyclone steadily weakened and is estimated to have merged with another low by 0600 UTC 6 September over the Labrador Sea."

7.2.2 Hurricane Isaac

Text extracted from Berg (2013)

"Isaac originated from a tropical wave that moved off the coast of Africa on 16 August. A broad area of low pressure developed along the tropical wave axis south of the Cape Verde Islands on 17 August, but the low did not develop a well-defined center of circulation until 1200 UTC 20 August over the central tropical Atlantic. Deep convection became sufficiently organized near the center of the low for the system to be classified as a tropical depression at 0600 UTC 21 August when it was centered about 625 n mi east of the Lesser Antilles. The depression strengthened and became a tropical storm 12 h later about 450 n mi east of the Lesser Antilles.

A strong deep-layer subtropical ridge over the western Atlantic caused Isaac to move quickly westward at 15 to 20 kt for the next two days. The center of the tropical storm moved through the Leeward Islands between the islands of Guadeloupe and Dominica between 1800

UTC 22 August and 0000 UTC 23 August, but the strongest winds were located well to the north of the center, spreading across the northern Leeward Islands and the Virgin Islands. Isaac continued generally westward over the eastern Caribbean Sea until early on 24 August, and aircraft and satellite data indicated that the structure of the cyclone became less organized when the low-level center reformed farther south and the circulation became more tilted. Nonetheless, Isaac strengthened to an intensity of 55 kt on 24 August when it turned northwestward toward Hispaniola. The structure of the cyclone began to improve with the formation of a more developed inner core and the first hints of an eye just before Isaac made landfall on the southern coast of Haiti near the city of Jacmel around 0600 UTC 25 August.

The center of Isaac quickly traversed the narrow southwestern peninsula of Haiti, and the cyclone weakened slightly when the circulation interacted with the mountainous terrain of Hispaniola. Isaac continued northwestward over the Gulf of Gonâve during the early morning hours of 25 August and moved just south of the Windward Passage, making landfall along the southeastern coast of Cuba near Cajobabo, Guantánamo, around 1500 UTC with maximum winds of 50 kt. The center emerged from the northern coast of Cuba into the Atlantic near Rafael Freyre, Holguín, around 2015 UTC. Isaac grew in size during its passage across Haiti and Cuba, with tropical-storm-force winds extending up to 180 n mi to the north of the center across the Turks and Caicos Islands and most of the Bahamas.

After emerging over the Atlantic, Isaac turned west-northwestward and moved faster on 26 August between a large deep-layer low over the northwestern Caribbean Sea and a midtropospheric ridge over the western Atlantic. Isaac had maximum sustained winds of 50 kt while the center moved parallel to the northern coast of Cuba toward the Straits of Florida, passing south of the Florida Keys later in the day. Tropical-storm-force winds, especially in gusts, affected the Florida Keys and South Florida in rain bands that moved across the area for much of the day.

Isaac entered the southeastern Gulf of Mexico early on 27 August, moving more slowly toward the west-northwest and northwest as it reached the southwestern periphery of the subtropical ridge. The wind field remained large, and microwave data indicated that deep convection became more organized in a ring around the center of circulation. Isaac gradually strengthened while moving across the Gulf of Mexico and became a hurricane around 1200 UTC 28 August while centered about 75 n mi southeast of the mouth of the Mississippi River. A midlevel blocking ridge to the northwest of the hurricane caused Isaac to slow down considerably while it approached the coast of Louisiana, which prolonged the strong winds, dangerous storm surge, and heavy rains along the northern Gulf coast. Isaac made its first landfall along the coast of Louisiana at Southwest Pass on the mouth of the Mississippi River around 0000 UTC 29 August with maximum sustained winds of 70 kt. The center then wobbled westward back over water and made a second landfall just west of Port Fourchon, Louisiana, around 0800 UTC 29 August.

Isaac gradually weakened once it moved inland over southeastern Louisiana, and it became a tropical storm at 1800 UTC 29 August when the center was located about 35 n mi west-southwest of New Orleans. A mid-level anticyclone over the southeastern United States steered Isaac northwestward across Louisiana on 30 August, and the cyclone weakened to a tropical depression around 0000 UTC 31 August just after crossing into southern Arkansas. The depression turned northward and moved into extreme southwestern Missouri later on 31 August. The center of circulation then lost its definition over western Missouri early on 1 September, and Isaac dissipated just after 0600 UTC about 55 n mi west-southwest of Jefferson City, Missouri. The remnants of Isaac moved northeastward and eastward across Missouri and Illinois, producing several tornadoes across the Mississippi River Valley later on 1 September."

7.2.3 Hurricane Michael

Text extracted from Kimberlain and Zelinsky (2012).

"Michael formed from a non-tropical weather system. A mid- to upper-level shortwave disturbance, originating from a longwave trough over eastern North America, cut off southwest of the Azores on 30 August and began to move slowly southwestward. The low-level reflection of this feature, a swirl of low clouds embedded within a weak trough, was first noted on 1 September about 500 n mi southwest of the Azores. Over the next day, sporadic convection caused the low-level swirl and trough to consolidate despite moderate northwesterly shear as it moved toward the southwest underneath a northeast-to-southwest oriented ridge. A small but well-defined low pressure area formed around 0000 UTC 2 September about 730 n mi southwest of the Azores. By 0600 UTC 3 September, the low pressure area attained enough persistent convective organization to be classified as a tropical depression.

The forward speed of the depression decreased, and the heading turned, first toward the west and then toward the northwest, as the western extension of the ridge weakened ahead of a mid-latitude trough approaching from the west on 3 September. The approaching trough also caused the deep-layer vertical wind shear to shift to the southwest and lessen somewhat, allowing convection to develop closer to the center. Strengthening began shortly after the decrease in shear, and the system became a tropical storm at 0600 UTC 4 September about 1075 n mi southwest of the Azores. Michael entered a region of weak steering flow well ahead of the same trough, and the tropical storm slowed further before turning toward the northeast. Late on 4 September, the vertical wind shear decreased further, allowing the circulation to become vertically aligned. At the same time, microwave data confirmed the existence of a closed ring of shallow convection around the center. Strongly divergent upper-level flow over Michael associated with the upper-level trough helped to enhance the outflow of the tropical storm, and a period of rapid intensification (a 30 kt or greater intensity increase in a 24-h period) began around 1200 UTC 5 September. During the next 24 h, the estimated intensity of Michael increased by 50 kt as the cyclone accelerated toward the northeast ahead of the trough. The hurricane reached its peak intensity of 100 kt while

centered about 890 n mi west-southwest of the Azores at 1200 UTC 6 September.

Shortly after reaching peak intensity, the small cyclone developed a concentric eyewall, which resulted in an increase in the eye diameter and the beginning of period of weakening. In addition, the mid-latitude trough passed to the north of Michael later on 6 September, ending the favorable upper-level pattern. Michael began to experience northwesterly shear in the wake of the trough, which led to the erosion of convection in the northwest quadrant of the cyclone (Fig. 4) and additional weakening as the hurricane slowed down and turned back toward the northwest. As the mid-latitude trough continued to move away from the hurricane early on 8 September, the wind shear decreased, allowing deep convection to once again wrap around the center. Michael is estimated to have reached a secondary peak of 90 kt at 1800 UTC 8 September about 800 n mi west-southwest of the Azores. This second intensification phase was short-lived, however, as Michael was steered westward on 9 September, under the influence of a mid-level shortwave ridge that developed over the central Atlantic between Leslie and Michael. As Michael moved around the ridge, the outflow of Hurricane Leslie led to an increase in northerly vertical wind shear. In addition, dry air, originating from the subsident region behind the once helpful mid-latitude trough, wrapped around the center and was entrained into the inner core, helping to erode the deep convection.

As a result of these negative factors, the mid-level center of Michael became displaced to the south of the low-level center on 10 September. Michael weakened to a tropical storm around 0000 UTC 11 September as the low-level center became exposed and accelerated northward ahead of a deep-layer trough over the eastern United States. By 1200 UTC 11 September, the circulation was devoid of deep convection. Michael became a remnant low at 1800 UTC 11 September. The remnant low continued to accelerate to the northeast until it was absorbed by a front at 1200 UTC 12 September, about 820 n mi northwest of the Azores."

7.2.4 Hurricane Ingrid

Text extracted from Beven II (2014).

"The origin of Ingrid was complicated. One contributor was a tropical wave that moved westward from the coast of Africa on 28 August and showed little distinction through 1 September. On 2 September, shower activity increased near the northern end of the wave axis. This area of weather would eventually be absorbed into Tropical Storm Gabrielle, which was developing near and north of Puerto Rico during the 3 - 7 September period. The southern part of the wave continued westward and eventually moved into a large area of low-level cyclonic flow extending from the western Caribbean Sea across Central America into the eastern north Pacific. The combination of this flow and the wave produced two areas of disturbed weather between 8-10 September. One, over the Pacific, moved westward and eventually helped spawn Hurricane Manuel. The second, which appeared over the northwestern Caribbean Sea on 9 September, became Ingrid.

Slow development of the Caribbean disturbance led to formation of a low pressure area on 11 September. While the system showed signs of organization before moving over the Yucatan Peninsula later that day, surface observations indicate that it had not developed into a tropical cyclone. The low moved west-northwestward, with the center apparently reforming over the Bay of Campeche early on 12 September. Subsequent development led to the formation of a tropical depression around 1800 UTC that day about 150 n mi east-northeast of Veracruz, Mexico.

The depression initially moved westward, but turned toward the west-southwest on 13 September while the cyclone intensified into a tropical storm. Later that day, Ingrid made a hairpin turn when it was centered about 50 n mi east of Veracruz. On 14 September a combination of a mid/upper-level trough over northeastern Mexico and low/mid-level ridging over the southeastern United States steered Ingrid north-northeastward and then northward. Although the trough and upper-level outflow from Manuel caused moderate westerly vertical wind shear over Ingrid, the cyclone managed to intensify into

a hurricane later on 14 September. Thereafter, it reached a peak intensity of 75 kt early on 15 September while centered about 215 n mi southeast of La Pesca, Mexico.

The hurricane turned northwestward near the time of peak intensity, and this motion continued for the rest of the day. On 16 September, a mid-level ridge over Texas caused Ingrid to turn west-northwestward. Increasing vertical shear caused the cyclone to weaken below hurricane strength, and it is estimated that the maximum winds had decreased to 55 kt when the center made landfall just south of La Pesca around 1115 UTC that day. After landfall, Ingrid moved slowly westward until it dissipated over northeastern Mexico on 17 September."

8 Bibliography

Anthes, R. A.: Data Assimilation and Initialization of Hurricane Prediction Models, J. Atmos. Sci., 31(3), 702–719, doi:10.1175/1520-0469(1974)031<0702:DAAIOH>2.0.CO;2, 1974.

Bell, R. S.: The Meteorological Office fine-mesh data assimilation scheme, Meteorol. Mag., 115(1367), 161–177 [online] Available from: papers://2ae67f3f-e008-4816-adce-b312905b08fd/Paper/p124, 1986.

Berg, P., Döscher, R. and Koenigk, T.: Impacts of using spectral nudging on regional climate model RCA4 simulations of the Arctic, Geosci. Model Dev., 6(3), 849–859, doi:10.5194/gmd-6-849-2013, 2013.

Berg, R.: National Hurricane Center Tropical Cyclone Report: Hurricane Isaac (2012)., 2013.

Van Den Besselaar, E. J. M., Haylock, M. R., Van Der Schrier, G. and Klein Tank, A. M. G.: A European daily high-resolution observational gridded data set of sea level pressure, J. Geophys. Res. Atmos., 116(11), D11110, doi:10.1029/2010JD015468, 2011.

Beven II, J. L.: National Hurricane Center Tropical Cyclone Report: Hurricane Ingrid (2013)., 2014.

Braun, M., Caya, D., Frigon, A. and Slivitzky, M.: Internal Variability of the Canadian RCM's Hydrological Variables at the Basin Scale in Quebec and Labrador, J. Hydrometeorol., 13(2), 443–462, doi:10.1175/JHM-D-11-051.1, 2012.

Cangialosi, J. P.: National Hurricane Center Tropical Cyclone Report: Hurricane Earl (2010)., 2011.

Choi, S. J. and Lee, D. K.: Impact of spectral nudging on the downscaling of tropical cyclones in regional climate simulations, Adv.

Atmos. Sci., 33(6), 730–742, doi:10.1007/s00376-016-5061-y, 2016.

Colin, J., DéQué, M., Radu, R. and Somot, S.: Sensitivity study of heavy precipitation in Limited Area Model climate simulations: Influence of the size of the domain and the use of the spectral nudging technique, Tellus, Ser. A Dyn. Meteorol. Oceanogr., 62(5), 591–604, doi:10.1111/j.1600-0870.2010.00467.x, 2010.

Davies, H. C.: A lateral boundary formulation for multi-level prediction models, Q. J. R. Meteorol. Soc., 102(432), 405–418, doi:10.1002/qj.49710243210, 1976.

Davies, H. C.: Limitations of Some Common Lateral Boundary Schemes used in Regional NWP Models, Mon. Weather Rev., 111(5), 1002–1012, doi:10.1175/1520-0493(1983)111<1002:LOSCLB>2.0.CO;2, 1983.

Davies, H. C. and Turner, R. E.: Updating prediction models by dynamical relaxation: an examination of the technique, Q. J. R. Meteorol. Soc., 103(436), 225–245, doi:10.1002/qj.49710343602, 1977.

Dudhia, J.: Numerical Study of Convection Observed during the Winter Monsoon Experiment Using a Mesoscale Two-Dimensional Model, J. Atmos. Sci., 46(20), 3077–3107, doi:10.1175/1520-0469(1989)046<3077:NSOCOD>2.0.CO;2, 1989.

de Elía, R. and Côté, H.: Climate and climate change sensitivity to model configuration in the Canadian RCM over North America, Meteorol. Zeitschrift, 19(4), 325–339, doi:10.1127/0941-2948/2010/0469, 2010.

de Elía, R., Caya, D., Côté, H., Frigon, A., Biner, S., Giguère, M., Paquin, D., Harvey, R. and Plummer, D.: Evaluation of uncertainties in the CRCM-simulated North American climate, Clim. Dyn., 30(2–3), 113–132, doi:10.1007/s00382-007-0288-z, 2008.

Errico, R. M.: Spectra Computed from a Limited Area Grid, Mon.

Weather Rev., 113(9), 1554–1562, doi:10.1175/1520-0493(1985)113<1554:SCFALA>2.0.CO;2, 1985.

Gill, A. E.: Atmosphere-Ocean Dynamics, Academic Press., 1982.

Gómez, B. and Miguez-Macho, G.: The impact of wave number selection and spin-up time in spectral nudging, Q. J. R. Meteorol. Soc., 143(705), 1772–1786, doi:10.1002/qj.3032, 2017.

Haylock, M. R., Hofstra, N., Klein Tank, A. M. G., Klok, E. J., Jones, P. D. and New, M.: A European daily high-resolution gridded data set of surface temperature and precipitation for 1950-2006, J. Geophys. Res. Atmos., 113(20), D20119, doi:10.1029/2008JD010201, 2008.

Hong, S.-Y. and Lim, J.-O. J.: The WRF Single-Moment 6-Class Microphysics Scheme (WSM6), J. Korean Meteorol. Soc., 2(42), 129–151, 2006.

Hong, S.-Y., Noh, Y. and Dudhia, J.: A New Vertical Diffusion Package with an Explicit Treatment of Entrainment Processes, Mon. Weather Rev., 134(9), 2318–2341, doi:10.1175/MWR3199.1, 2006.

Huffman, G. J., Bolvin, D. T., Nelkin, E. J., Wolff, D. B., Adler, R. F., Gu, G., Hong, Y., Bowman, K. P. and Stocker, E. F.: The TRMM Multisatellite Precipitation Analysis (TMPA): Quasi-Global, Multiyear, Combined-Sensor Precipitation Estimates at Fine Scales, J. Hydrometeorol., 8(1), 38–55, doi:10.1175/JHM560.1, 2007.

Hunter, J. D.: Matplotlib: A 2D Graphics Environment, Comput. Sci. Eng., 9(3), 90–95, doi:10.1109/MCSE.2007.55, 2007.

International Satellite Cloud Climatology Project: Cloud Climatology: Global Distribution and Character of Clouds, [online] Available from: https://www.giss.nasa.gov/research/briefs/rossow_01/distrib.html (Accessed 16 January 2019), n.d.

Jung, T. and Leutbecher, M.: Scale-dependent verification of ensemble forecasts, Q. J. R. Meteorol. Soc., 134(633 B), 973–984,

doi:10.1002/qj.255, 2008.

Kain, J. S.: The Kain–Fritsch Convective Parameterization: An Update, J. Appl. Meteorol., 43(1), 170–181, doi:10.1175/1520-0450(2004)043<0170:TKCPAU>2.0.CO;2, 2004.

Katavouta, A. and Thompson, K. R.: Downscaling ocean conditions: Experiments with a quasi-geostrophic model, Ocean Model., 72, 231–241, doi:10.1016/j.ocemod.2013.10.001, 2013.

Kimberlain, T. B. and Zelinsky, D. A.: National Hurricane Center Tropical Cyclone Report: Hurricane Michael (2012)., 2012.

Liu, P., Tsimpidi, A. P., Hu, Y., Stone, B., Russell, A. G. and Nenes, A.: Differences between downscaling with spectral and grid nudging using WRF, Atmos. Chem. Phys., 12(8), 3601–3610, doi:10.5194/acp-12-3601-2012, 2012.

Lucas-Picher, P., Somot, S., Déqué, M., Decharme, B. and Alias, A.: Evaluation of the regional climate model ALADIN to simulate the climate over North America in the CORDEX framework, Clim. Dyn., 41(5–6), 1117–1137, doi:10.1007/s00382-012-1613-8, 2013.

Lyne, W. H., Swinbank, R. and Birch, N. T.: A data assimilation experiment and the global circulation during the FGGE special observing periods, Q. J. R. Meteorol. Soc., 108(457), 575–594, doi:10.1002/qj.49710845706, 1982.

Meinke, I., Geyer, B., Feser, F. and von Storch, H.: The impact of spectral nudging on cloud simulation with a regional atmospheric model, J. Atmos. Ocean. Technol., 23(6), 815–824, doi:10.1175/JTECH1879.1, 2006.

Miguez-Macho, G., Stenchikov, G. L. and Robock, A.: Spectral nudging to eliminate the effects of domain position and geometry in regional climate model simulations, J. Geophys. Res. D Atmos., 109(13), n/a-n/a, doi:10.1029/2003JD004495, 2004.

Miguez-Macho, G., Stenchikov, G. L. and Robock, A.: Regional climate simulations over North America: Interaction of local processes with improved large-scale flow, J. Clim., 18(8), 1227–1246, doi:10.1175/JCLI3369.1, 2005.

Mlawer, E. J., Taubman, S. J., Brown, P. D., Iacono, M. J. and Clough, S. A.: Radiative transfer for inhomogeneous atmospheres: RRTM, a validated correlated-k model for the longwave, J. Geophys. Res. Atmos., 102(D14), 16663–16682, doi:10.1029/97JD00237, 1997.

Omrani, H., Drobinski, P. and Dubos, T.: Optimal nudging strategies in regional climate modelling: Investigation in a Big-Brother experiment over the European and Mediterranean regions, Clim. Dyn., 41(9–10), 2451–2470, doi:10.1007/s00382-012-1615-6, 2013.

Radu, R., Déqué, M. and Somot, S.: Spectral nudging in a spectral regional climate model, in Tellus, Series A: Dynamic Meteorology and Oceanography, vol. 60, pp. 898–910, Taylor & Francis., 2008.

Sanchez-Gomez, E., Somot, S. and Déqué, M.: Ability of an ensemble of regional climate models to reproduce weather regimes over Europe-Atlantic during the period 1961-2000, Clim. Dyn., 33(5), 723–736, doi:10.1007/s00382-008-0502-7, 2009.

Schraff, C. H.: Data assimilation and mesoscale weather prediction: A study with a forecast model for the Alpine Region, Swiss Meteorol. Inst., 56, doi:10.3929/ETHZ-A-001658957, 1996.

Schraff, C. H.: Mesoscale data assimilation and prediction of low stratus in the Alpine region, Meteorol. Atmos. Phys., 64(1–2), 21–50, doi:10.1007/BF01044128, 1997.

Separovic, L., de Elía, R. and Laprise, R.: Impact of spectral nudging and domain size in studies of RCM response to parameter modification, Clim. Dyn., 38(7–8), 1325–1343, doi:10.1007/s00382-011-1072-7, 2012.

Skamarock, W. C. and Klemp, J. B.: A time-split nonhydrostatic

atmospheric model for weather research and forecasting applications, J. Comput. Phys., 227(7), 3465–3485, doi:10.1016/j.jcp.2007.01.037, 2008.

Skamarock, W. C., Klemp, J. B., Dudhi, J., Gill, D. O., Barker, D. M., Duda, M. G., Huang, X.-Y., Wang, W. and Powers, J. G.: A Description of the Advanced Research WRF Version 3. NCAR Technical Note NCAR/TN-475+STR., 2008.

Stacey, M. W., Shore, J., Wright, D. G. and Thompson, K. R.: Modeling events of sea-surface variability using spectral nudging in an eddy permitting model of the northeast Pacific Ocean, J. Geophys. Res. Ocean., 111(6), 1–8, doi:10.1029/2005JC003278, 2006.

Stauffer, D. R. and Seaman, N. L.: Use of Four-Dimensional Data Assimilation in a Limited-Area Mesoscale Model. Part I: Experiments with Synoptic-Scale Data, Mon. Weather Rev., 118(6), 1250–1277, doi:10.1175/1520-0493(1990)118<1250:UOFDDA>2.0.CO;2, 1990.

Stauffer, D. R. and Seaman, N. L.: Multiscale Four-Dimensional Data Assimilation, J. Appl. Meteorol., 33(3), 416–434, doi:10.1175/1520-0450(1994)033<0416:MFDDA>2.0.CO;2, 1994.

Stauffer, D. R., Seaman, N. L. and Binkowski, F. S.: Use of Four-Dimensional Data Assimilation in a Limited-Area Mesoscale Model Part II: Effects of Data Assimilation within the Planetary Boundary Layer, Mon. Weather Rev., 119(3), 734–754, doi:10.1175/1520-0493(1991)119<0734:UOFDDA>2.0.CO;2, 1991.

von Storch, H., Langenberg, H. and Feser, F.: A Spectral Nudging Technique for Dynamical Downscaling Purposes, Mon. Weather Rev., 128(10), 3664–3673, doi:10.1175/1520-0493(2000)128<3664:ASNTFD>2.0.CO;2, 2000.

Vincent, C. L. and Hahmann, A. N.: The impact of grid and spectral nudging on the variance of the near-surface wind speed, J. Appl. Meteorol. Climatol., 54(5), 1021–1038, doi:10.1175/JAMC-D-14-

0047.1, 2015.

Waldron, K. M., Paegle, J. and Horel, J. D.: Sensitivity of a Spectrally Filtered and Nudged Limited-Area Model to Outer Model Options, Mon. Weather Rev., 124(3), 529–547, doi:10.1175/1520-0493(1996)124<0529:SOASFA>2.0.CO;2, 1996.

Wang, H., Wang, Y. and Xu, H.: Improving simulation of a tropical cyclone using dynamical initialization and large-scale spectral nudging: A case study of Typhoon Megi (2010), Acta Meteorol. Sin., 27(4), 455–475, doi:10.1007/s13351-013-0418-y, 2013.

Wang, J. and Kotamarthi, V. R.: Assessment of dynamical downscaling in near-surface fields with different spectral nudging approaches using the nested regional climate model (NRCM), J. Appl. Meteorol. Climatol., 52(7), 1576–1591, doi:10.1175/JAMC-D-12-0302.1, 2013.

Yamaguchi, T., Brewer, W. A. and Feingold, G.: Evaluation of Modeled Stratocumulus-Capped Boundary Layer Turbulence with Shipborne Data, J. Atmos. Sci., 70(12), 3895–3919, doi:10.1175/JAS-D-13-050.1, 2013.